Biased activation of the vasopressin V2 receptor probed by NMR, paramagnetic ligands, and molecular dynamics simulations.

Gérald Gaibelet,[†,$,#] Aurélien Fouillen,[†,⁋,#] Stéphanie Riché,[‡] Hélène Orcel,[†] Christiane Mendre,[†] Romain Lanotte,[†] Julie N'Guyen,[†] Rémy Sounier,[†] Sébastien Granier,[†] Dominique Bonnet,[‡] Xiaojing Cong,[†,*] Bernard Mouillac,[†,*] Hélène Déméné[⁋,*]

[†]Institut de Génomique Fonctionnelle, Université de Montpellier, CNRS, INSERM, 34094 Montpellier cedex 5, France.

[⁋]Centre de Biologie Structurale, Univ Montpellier, INSERM, CNRS, 34090 Montpellier, France

[‡] Laboratoire d'Innovation Thérapeutique, UMR7200 CNRS, Université de Strasbourg, Institut du Médicament de Strasbourg, 67412 Illkirch-Graffenstaden, France.

[$] Present address, AB Science, 13288 Marseille cedex 9, France

[#] These authors contributed equally to the work.

KEYWORDS: GPCR dynamics, biased activation, tolvaptan, MCF14, arginine vasopressin, enhanced sampling, NMR sensors, TEMPOL.

ABSTRACT: G protein-coupled receptors (GPCRs) control critical intercellular communications by responding to extracellular stimuli and undertaking conformational changes to convey disparate signals to intracellular effectors. We combined NMR, molecular pharmacology, and enhanced sampling molecular dynamics (MD) simulations to study the conformational diversity of the vasopressin V2 receptor (V2R) bound to different types of ligands: the antagonist tolvaptan, the endogenous unbiased agonist arginine-vasopressin, and MCF14, a Gs-protein biased agonist. We developed a double-labeling NMR scheme to study the conformational dynamics: V2R was subjected to lysine $^{13}CH_3$ methylation, whereas the agonists were tagged with a paramagnetic probe. Paramagnetic relaxation enhancements were used to validate the ligand binding poses in the MD simulations. We found that the bias for the Gs protein over the β-arrestin pathway involves interactions between the conserved NPxxY motif in the transmembrane helix (TM) 7 and a central hydrophobic patch in TM3, which constrains TM7 and likely inhibits β-arrestin signaling. A similar mechanism was observed for the naturally occurring V2R mutation, I130$^{3.43}$N, which constitutively activates the Gs protein without concomitant β-arrestin recruitment. This mechanism resembles previous findings on the μ-opioid receptor and indicate common patterns in class A GPCRs.

INTRODUCTION

G-protein coupled receptors (GPCRs) are the largest protein family in the human genome and key players in cell signaling. As such, they comprise the targets of ca. 40% of marketed drugs.[1,2] As transmembrane receptors, they sense extracellular stimuli and trigger signal transduction cascades inside the cell, principally via the G protein and the β-arrestin (βArr) pathways.[3] Stimulation of G proteins can activate second messengers and modulate receptor kinases and ion channels. βArrs control the desensitization, internalization, and recycling of GPCRs. They act as multifunctional scaffolds that interact with many protein partners and protein kinases, thereby leading to the phosphorylation of numerous intracellular targets. GPCR ligands may preferentially modulate some of the signaling pathways over the others, resulting in different cellular outcomes. This functional selectivity is known as GPCR ligand bias. [4] It enables better control of drug therapeutic effects, opening a new avenue to drug discovery. GPCR biased signaling may even occur in the *apo* state, in certain constitutively active (often pathological) mutants.[5,6]

X-ray crystallography and cryo-electron microscopy (cryo-EM) have revealed remarkably unified structural rearrangements upon class A GPCR activation stabilized by G proteins/arrestins/nanobodies, characterized by a large outward displacement of the transmembrane helix 6 (TM6) and smaller inward movements of TM7.[7–11] Activation involves rearrangements of conserved microswitches such as the Na^+ anchor D$^{2.50}$ in TM2 (superscript refers to Ballesteros-Weinstein nomenclature)[12], DR$^{3.50}$Y in TM3, CW$^{6.48}$xP and PI$^{3.40}$F in TM3-TM5-TM6, and NP$^{7.50}$xxY in TM7. However, receptor conformational changes before coupling with intracellular partners which are essential for biased signaling, are highly dynamic and poorly understood. Biased signaling roots in the conformational plasticity of GPCRs.[3] Ligand and mutations can differentially alter GPCR conformational dynamics and affect the receptor signaling profile. Yet, the structural mechanisms underlying biased signaling remain largely elusive, which consequently hinders the clinical translation. Of note, spectroscopies in solution have provided valuable information. Biased signaling may originate from transient activation states that favor G protein over arrestin binding, via differential TM conformations[13–16] and/or concerted movements.[17–20] Molecular dynamics (MD) simulations have also proven effective in studying detailed receptor conformational dynamics involved in activation, inhibition, or biased signaling.[17,21–23] Here, we combine solution NMR and MD simulations to investigate the biased activation mechanism of V2R.

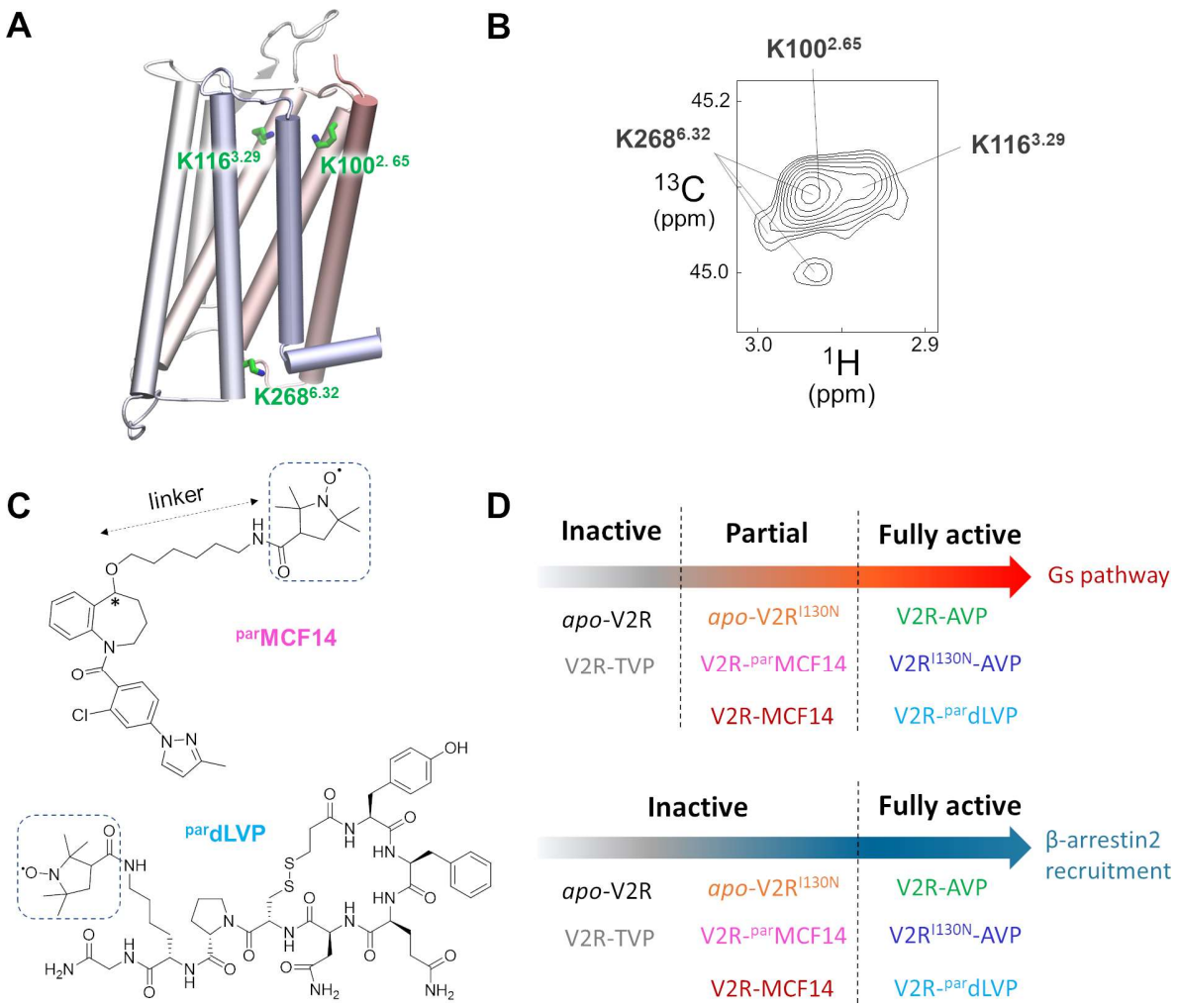

Figure 1. NMR labels, paramagnetic probes, and functional profiles of the systems studied. (A) Three lysine sensors in the inactive-state model of V2R. **(B)** Peak assignments in the NMR spectra of $^{13}CH_3$-Lys-V2R. K100$^{2.65}$ and K116$^{3.29}$ each show one peak, whereas K268$^{6.32}$ displays 3 peaks. **(C)** Chemical structures of the paramagnetic agonists. The paramagnetic tags are boxed. The chiral center of ^{par}MCF14 is labeled by an asterisk. **(D)** Systems studied in the MD simulations. The functional profile of each system toward the two main signaling pathways of V2R, Gs activation and βArr2 recruitment, is also listed in Table 2.

V2R is a class A GPCR that regulates the renal antidiuretic response in mammals.[24] Binding of arginine-vasopressin (AVP) to V2R activates both the Gs protein and the βArr pathways. The former leads to water reabsorption and urine concentration,[24] whereas the latter is associated with cell growth and proliferation.[25,26] V2R is a major therapeutic target for many water balance disorders.[27] Moreover, genetic diseases caused by pathogenic V2R mutations indicate the importance of signaling bias for future drug development. On one hand, loss-of-function mutations result in the congenital nephrogenic diabetes insipidus (cNDI),[28] characterized by excessive urine voiding, dehydration, thirst, and hypernatremia.[29] In most cases, the mutant receptors are misfolded and retained in the endoplasmic reticulum.[30] A class of benzazepine compounds, the MCF series of biased agonists, have been found to rescue some of the cNDI mutant's membrane expression and signaling. They display a promising biased profile of long-lasting activation of the Gs protein pathway, without triggering βArr-mediated internalization.[31] On the other hand, gain-of-function V2R mutations lead to the nephrogenic syndrome of inappropriate antidiuresis (NSIAD), characterized by hyponatremia due to impaired free water excretion despite undetectable plasma AVP levels.[32] Several of these mutants, such as I130$^{3.43}$N, display constitutive activities for the Gs protein but not the βArrs.[33–35]

Understanding the molecular mechanisms of V2R biased activation represents a major step toward better characterization of the pathophysiology of V2R-associated disorders and the development of next-generation therapeutics. Due to its conformational flexibility, high-resolution V2R structures have only been obtained recently by us and two other groups, in active state in complex with AVP and the Gs [36–38] or the βArr1 signaling proteins.[39] No structure of V2R is yet available in an inactive state or bound to small-molecule ligands. Hence, little is known about V2R ligand bias or the ligand-/mutation-induced activation dynamics. We have previously found that AVP and the Gs-biased agonist MCF14 induced distinct V2R conformations on the intracellular side of TM7 and helix 8 (H8), using fluorophore sensors introduced in

these domains of the receptor.[16] In the present study, we combine functional pharmacology in living cells, solution NMR spectroscopy, and enhanced-sampling MD simulations to identify more precisely and comprehensively the V2R conformations associated with the Gs-biased agonist MCF14, in comparison with the unbiased agonist AVP, and the antagonist tolvaptan (TVP). To assess the ligand binding poses, we developed a double-labeling scheme using lysine $^{13}CH_3$ methylation on V2R and paramagnetic tagging of the ligands. The Paramagnetic relaxation enhancement (PRE) data were in agreement with the distances measured in the MD simulations with the tagged ligands. In addition, we identified distinct receptor conformations associated with the Gs-biased agonist and the constitutively Gs-active mutant, I130$^{3.43}$N, suggesting a biased activation mechanism involving the central hydrophobic patch in TM3 and the NP$^{7.50}$xxY motif in TM7.

RESULTS

Development of NMR sensors and paramagnetic ligands. To characterize the conformational changes of V2R upon ligand binding, we introduced sensors by methylating its lysines with two $^{13}CH_3$ groups, to be monitored by heteronuclear ^{1}H-^{13}C NMR, as described previously.[40,41] The V2R construct used here was truncated at the N- and C-termini and thus has three lysines, K100$^{2.65}$, K116$^{3.29}$ and K268$^{6.32}$, which were dimethylated (Figures 1A and S1A). K100$^{2.65}$ lies on the rim of the orthosteric pocket, whereas K116$^{3.29}$ is located within the pocket. K268$^{6.32}$ belongs to the cytoplasmic extremity of TM6, which makes it an appropriate sensor of the canonical activation, considering the pivotal role of TM6 therein.[10,11,37–39]

Table 1. Ligand affinity and potency in living cells[a]

	Ki (nM)[b,c]	EC50 (nM)[b]	
		cAMP	βArr2
AVP	0.93 ± 0.3 (n=5)	0.11 ± 0.01	0.85 ± 0.10
^{par}dLVP	273.5 ± 39.7	37.5 ± 3.2	110.5 ± 18
MCF14	7.9 ± 2.3	40.9 ± 11.6	n.a.[d]
^{par}MCF14	169.7± 24.7	647.6 ± 37 (n=5)	n.a.

[a]Measured in cells expressing the V2R construct used for NMR (Figure S1A).

[b]Values are mean ± SEM (n = 3, unless otherwise indicated).

[c]Dose-dependent competitive binding curves are provided in Figure 2.

[d]n.a.= not applicable

A representative heteronuclear ^{1}H-^{13}C HMQC spectrum of *apo* V2R is shown in Figure 1B. Peak assignments were obtained by site-directed mutagenesis of individual lysines into arginines (Figure S2). Contrary to K100$^{2.65}$ and K116$^{3.29}$ which have only one correlation peak, K268$^{6.32}$ is represented by a major peak and two minor correlation peaks, indicating conformational heterogeneity at the cytoplasmic end of TM6 in *apo* V2R.

Accurate prediction of the ligand binding pose is critical for meaningful MD simulations. Since i) only the AVP binding pose is known from the cryo-EM structures, and ii) the structures of TVP and MCF14 differ significantly from that of AVP (Figure S1B), we used ligand paramagnetic tagging to verify the ligand binding poses predicted by MD simulations. A TEMPOL group (Sigma) containing a nitroxide probe was covalently linked to MCF14 to obtain a paramagnetic form (^{par}MCF14) (Figures 1C, S1B and S3). PREs of the ^{1}H nuclei, a well-known source of long-range distance information, provide the distance estimation of TEMPOL to the methyl groups of K100$^{2.65}$ and K116$^{3.29}$, which can be compared directly with the MD simulations. To validate this approach, we first tested it on an AVP analog, the deaminated lysine vasopressin (dLVP), with the same paramagnetic tag (^{par}dLVP, Figures 1C, S1B and S3). We used dLVP to facilitate the chemical synthesis (Fig. S3), as it has been demonstrated to behave as LVP (the porcine homolog of AVP) and AVP towards V2R antidiuretic activity.[42] We verified that the paramagnetic tag did not alter the ligand signaling profiles in living cells, although the affinity and potency were reduced (Figure 2A and Table 1). Importantly, ^{par}dLVP is still a full unbiased agonist like AVP, whereas ^{par}MCF14 is a Gs-biased partial agonist like its parent compound.

Determination of ligand binding poses by combining NMR and MD. The PRE values were estimated by comparing the volumes of the V2R lysine correlation peaks in complex with the paramagnetic ligands, in the paramagnetic and diamagnetic states (Figure 2B). We used the K268$^{6.32}$R mutant V2R for this purpose, to obtain clear spectra of the K100$^{2.65}$ and K116$^{3.29}$ correlation peaks. We verified that the K268$^{6.32}$R mutation had negligible impacts on the ligand affinities and PREs compared to the wild-type (wt) receptor (Table S1 and Figures 2A and S4). Addition of the paramagnetic ligands induced a decrease in the peak volumes of K100$^{2.65}$ and K116$^{3.29}$ (Figure 2B), due to the distance-dependent relaxation effects of the unpaired ion in TEMPOL and the ligand-induced conformational changes.

Table 2. V2R systems studied.

Abbreviation	Ligand/ mutation	Gs activation	βArr2 recruitment
apo-V2R	n.a.[a]	-	-
V2R -AVP	AVP	+	+
V2R-^{par}dLVP	^{par}dLVP	+	+
V2R-MCF14	MCF14	+ (partial)	-
V2R-^{par}MCF14	^{par}MCF14	+ (partial)	-
V2R-TVP	Tolvaptan	-	-
apo-V2R^{I130N}	I130$^{3.43}$N	+ (constitutive)	-
V2R^{I130N}-AVP	AVP	+	+

[a] n.a.: not applicable.

Addition of 5 equivalents of ascorbic acid as reducing agent attenuated the interactions of the unpaired ion with the lysine nuclear spins, resulting in an increase of the lysine peak volumes. This effect was more remarkable on K100$^{2.65}$ than K116$^{3.29}$ for both ^{par}dLVP and ^{par}MCF14 (Figure 2B). Hence, the dimethylated side chain of K100$^{2.65}$ is, on average, closer to the paramagnetic center than that of K116$^{3.29}$ for both ligands.

The data above were compared with MD simulations of V2R-^{par}dLVP and V2R-^{par}MCF14 containing dimethylated lysines. The simulations were initiated with an inactive-state model of V2R (see Materials and Methods for details). ^{par}dLVP is a reference case to evaluate the method since it closely resembles AVP. ^{par}dLVP in the MD simulations maintained the same binding pose as that of AVP in the cryo-EM structures (Figure S5A).[38,39,43]

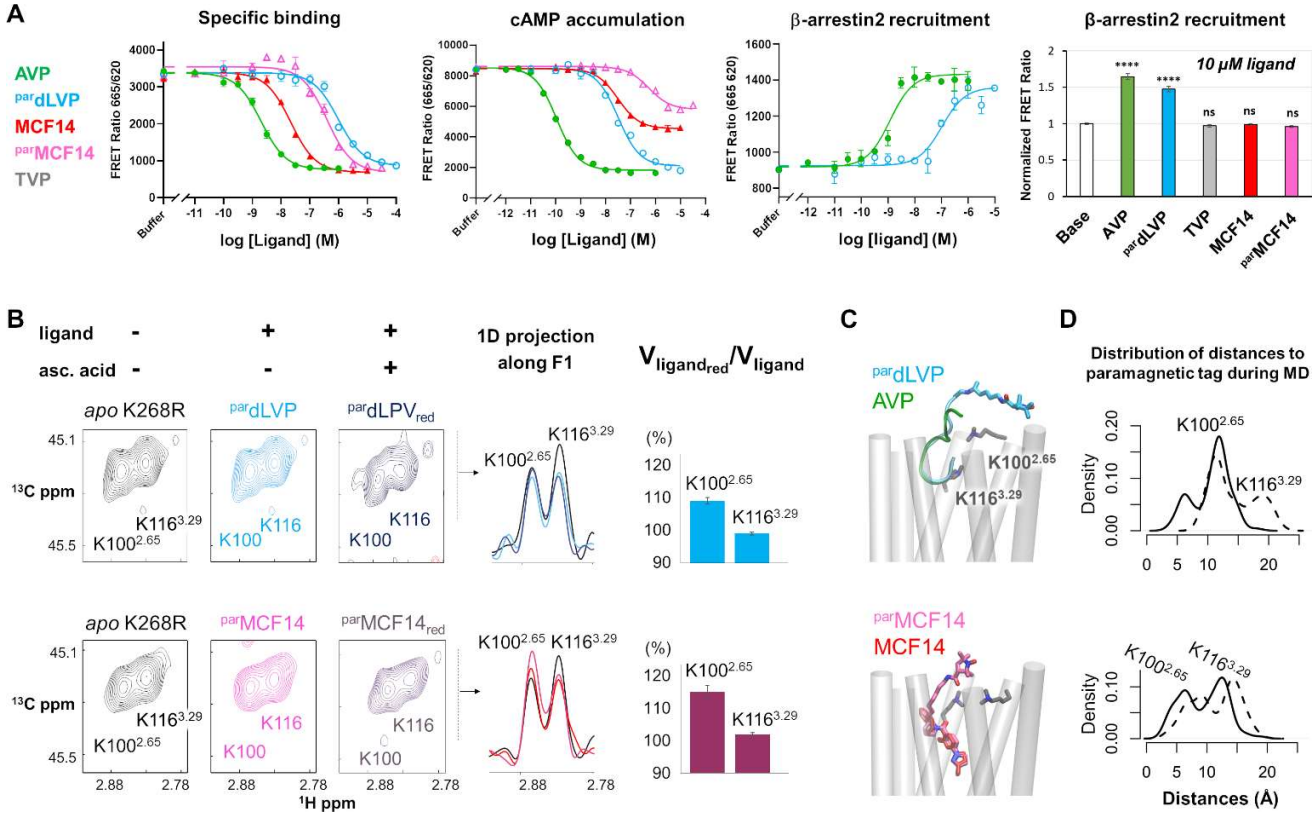

Figure 2. Pharmacological properties and binding poses of the ligands in V2R. (A) Specific ligand binding to V2R was measured by competitive binding against 5 nM of a fluorescent benzazepine-red antagonist. Dose-response curves of V2R-dependent Gs protein/adenylyl cyclase activation and recruitment of βArr2 to the adaptor protein AP2 were measured by the FRET ratio (665nm/620nm x 10,000). The cAMP accumulation which displaces the fluorescently-labelled cAMP binding to its specific antibody is shown in the presence of increasing concentrations of the ligands. MCF14 and ^{par}MCF14 showed no detectable βArr2 recruitment, like TVP, even at maximum concentration (10 μM, far-right panel). Data are mean ± SEM from 3 technical replicates. **(B)** Extracted HMQC spectra of K100$^{2.65}$ and K116$^{3.29}$ resonances of V2R K268$^{6.32}$R in apo form (black), or bound to ^{par}dLVP (sky blue) or ^{par}MCF14 (magenta), and reduced by ascorbic acid (royal blue and mauve taupe). The 1D projections along the ^{13}C dimension of ^{1}H rows are indicated by an arrow. For both ligands, ratios of peak volumes in the paramagnetic and diamagnetic (ligand$_{red}$) forms (right panel) show that paramagnetic tag affects the K100$^{2.65}$ peak stronger than that of K116$^{3.32}$, indicating shorter average distances between the TEMPOL nitroxide ion and the K100$^{2.65}$ methyl groups. Values are mean ± SEM of 2 technical replicates. **(C)** During the MD simulations, the paramagnetic tag was mobile in the extracellular solution and was on average closer to K100$^{2.65}$ than K116$^{3.32}$, consistent with the NMR spectra in (B). The tag did not alter the ligand binding poses. **(D)** Probability density distribution of the distances between the TEMPOL nitroxide ion and the methyl groups of K100$^{2.65}$ and K116$^{3.32}$ during the MD simulations.

The paramagnetic tag swayed at the entrance of the orthosteric pocket (Figure 2C). The paramagnetic center in ^{par}dLVP was on average closer to the K100$^{2.65}$ methyl groups than those of K116$^{3.29}$ (Figures 2D and S6), in line with the NMR measurements. In the case of ^{par}MCF14, the ligand used in the NMR studies was a mixture of two enantiomers (Figure 1B) and we examined both enantiomers in the MD simulations. R-^{par}MCF14 turned out to be highly mobile in the pocket during the simulations due to steric hindrance of the linker (Figure S5A), indicating low affinity. It was thus discarded. S-^{par}MCF14 was stable in the pocket and adopted the same binding pose as the untagged MCF14, suggesting that this enantiomer was the active one. Moreover, its paramagnetic center was closer to the K100$^{2.65}$ methyl groups than those of K116$^{3.29}$, in line with the NMR results (Figures 2D and S6). The paramagnetic ligands were slightly more mobile than their untagged counterparts during the simulations (Figure S5A), while maintaining the same binding pose (Figure 2C). This increase in mobility is consistent with their lower affinity than the untagged ligands in the cell assays. Therefore, the MD simulations were in good agreement with the NMR and the pharmacological data, confirming the reliability of the predicted ligand binding poses.

The antagonist TVP is also a mixture of two enantiomers (Figure S1). R-TVP and S-TVP behaved similarly during the MD simulations. Since R-TVP was slightly more stable in the V2R pocket (Figure S5), hereafter we refer to the simulation results of R-TVP as TVP. It showed a similar binding pose to MCF14 during the MD simulations (Figure 3A), which was expected given their chemical similarity. However, TVP formed three additional hydrogen bonds (H-bonds) with V2R (Figure 3A).

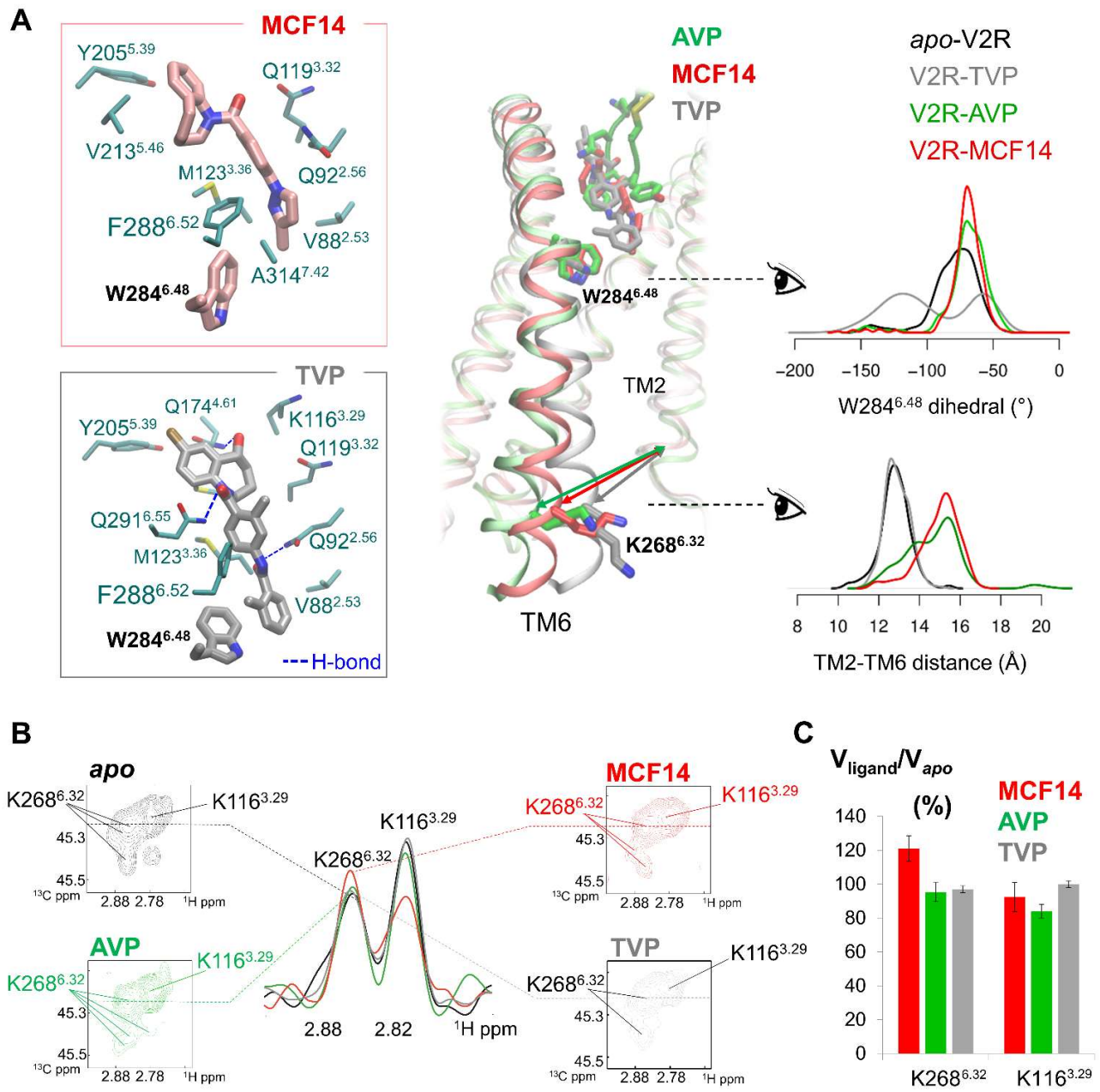

Figure 3.V2R conformational changes in TM6 induced by AVP, MCF14 and TVP. (A) MD simulations showed that MCF14 (Gs-biased agonist) and TVP (antagonist) adopted similar binding poses in the V2R orthosteric pocket. Residues within 3 Å distance of the ligands are shown in sticks. TVP altered the side-chain orientation of W284$^{6.48}$, and TM6 remained in the initial position close to TM2 on the intracellular side. MCF14 and AVP (unbiased agonist) stabilized the same W284$^{6.48}$ sidechain orientation (dihedral angle χ_2 around -70°) and led to TM6 opening on the intracellular side. TM2-TM6 distance was measured by the center-of-mass distance between the backbones of I74$^{2.39}$-F77$^{2.42}$ and V266$^{6.30}$-T269$^{6.33}$. **(B)** Extracted HMQC spectra of the K100$^{2.65}$R mutant in *apo* form (black) and in the presence of saturating concentrations of AVP (green), MCF14 (red) and TVP (gray). Minor and major peaks were impacted differently by the ligands. Minor peaks experienced chemical shift changes whereas major peaks experienced principally intensity variations. Dashed lines indicate the position of the cross-sections shown in the middle of panel B. These cross-sections demonstrate a sharpening of resonances in the AVP-bound state, compatible with the entropy loss compared to the *apo* form. Spectra represented in (B) were recorded on samples originating from the same batch of V2R culture and purification, except for TVP. The reference spectrum of *apo* V2R corresponding to the TVP-bound spectrum is shown in Figure S4. **(C)** Analysis of peak volume changes of the major peaks upon ligand binding compared to the *apo* form. K268$^{6.32}$ side chain exhibiteda distinct dynamical range in the MCF14-bound form, characterized by an increase in intensity and linewidth. Values are mean ± SEM of two (for AVP) or three (for MCF14) technical replicates. For TVP, errors were derived from the effect of random noise for the peak height estimated by the nlinS subroutine in the NMRPipe software.

Correlation of V2R conformational changes with ligand/mutation signaling profiles

Having determined the ligand binding poses, we analyzed the structural features associated with biased and unbiased V2R activation by solution NMR and MD simulation. In particular, among the eight simulations systems studied (Figure 1D and Table 2), we included the I130$^{3.43}$N mutant which was previously described to constitutively activate the Gs pathway,[33] consistent with our assay outcome (Figure S7). We also found that, as reported before,[33] upon AVP stimulation, the mutant could activate both the Gs and the βArr pathways, indicating that AVP overrides the mutational effect on the signaling preference (Figure S7). Therefore, the eight systems divide into three categories: inactive (*apo*-V2R and V2R-TVP), Gs activation (*apo*-I130N, V2R-MCF14 and V2R-^{par}MCF14), and unbiased activation (V2R-AVP, V2R-^{par}dLVP and I130N-AVP). All the simulations were performed in duplicates with dimethylated and natural lysines, starting from the inactive state. We found that lysine methylation introduced more fluctuations in the simulations without significant impacts on the receptor activation pattern. Therefore, hereafter we focus on the simulation results with natural lysines.

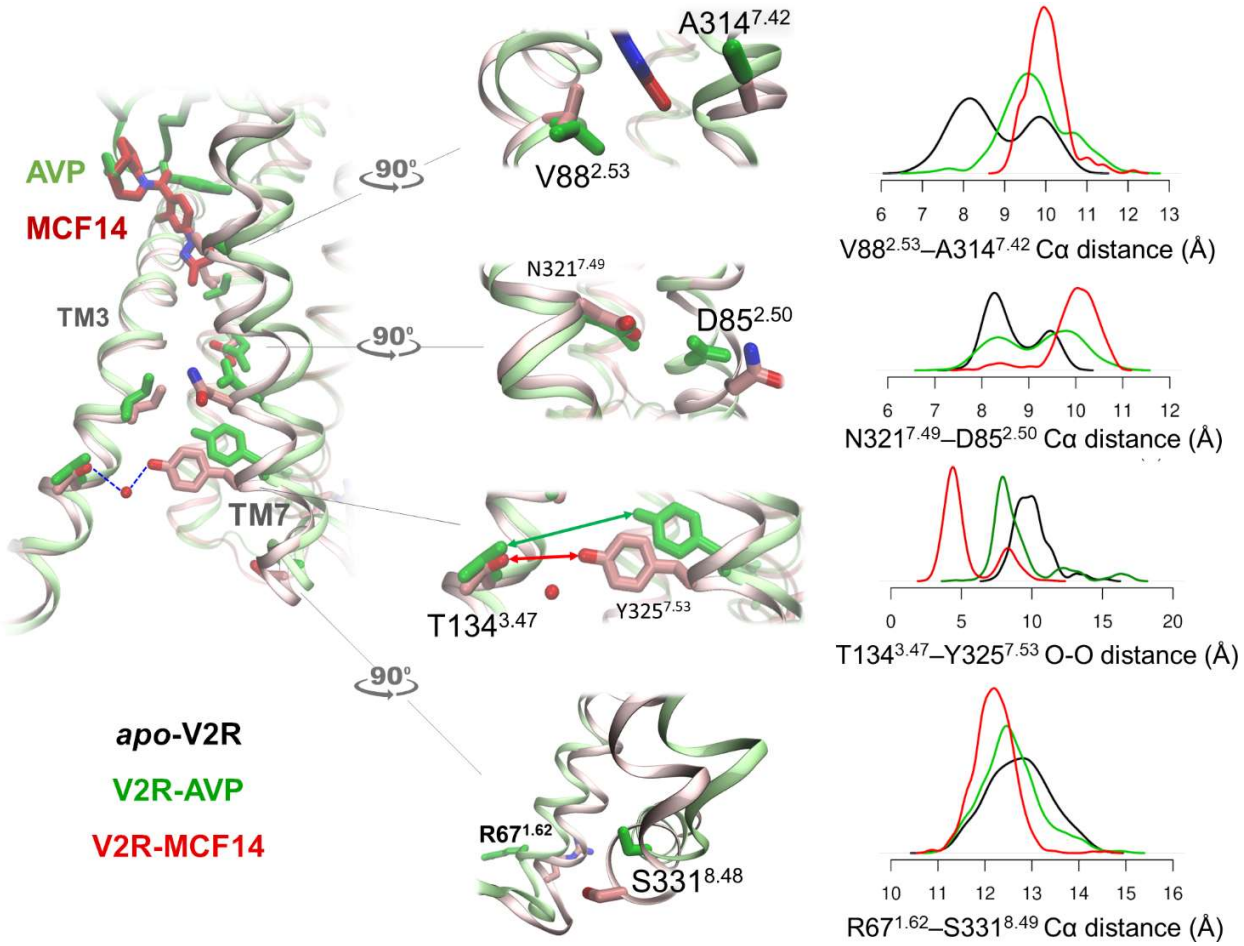

Figure 4. Proposed mechanism of G protein bias by MCF14. MCF14 inserts between TM2 and TM7, driving N321$^{7.49}$ to move away from D85$^{2.50}$ at the Na^+-binding site. Y325$^{7.53}$ moves toward TM3 and forms direct or water-mediated H-bonds with T134$^{3.47}$. H8 and TM1 become more compact on the intracellular side.

All the six systems in the activation category showed apparent TM6 outward movements with respect to TM2 on the cytoplasmic side (Figures 3A, S4B and S9A). V2R-AVP exhibited the highest flexibility and distinct conformational clusters at the intracellular end of TM6 (Figure S5B). By contrast, TVP stabilized TM6 in the initial inactive position, similar to *apo*-V2R. Moreover, TVP induced distinct orientations of W284$^{6.48}$ side chain contrasting all the other seven systems (Figures 3A and S9A). This was observed for both R-TVP and S-TVP (Figure S9A). W284$^{6.48}$ is part of the conserved CW$^{6.48}$xP motif in class A GPCRs, known as the "toggle switch" of receptor activation.[7] Therefore, TVP likely antagonizes V2R by blocking the conformational changes of this important activation switch. The TM6 movements observed in the MD simulations were in line with the changes in the NMR correlation peaks of K268$^{6.32}$. To observe clear signals of K268$^{6.32}$, we used the K100$^{2.65}$R mutant which preserves the signaling properties of wt V2R (Figure S8 and Table S2). In the *apo* form of the K100$^{2.65}$R mutant, K268$^{6.32}$ showed at least 3 resonance peaks, the main peak being also large and weak, indicating conformational heterogeneity at the intracellular end of TM6 (Figure 3B). Binding of the antagonist TVP caused no significant change compared to the *apo* form, in accordance with the MD simulations. By contrast, AVP

and MCF14 produced different spectral outputs. Binding to AVP resulted in a narrowing of the K116$^{3.29}$ and K268$^{6.32}$ (major) peaks, whereas the K268$^{6.32}$ minor peak (at 2.86/45.2 ppm) was split into two components of equal but weaker intensities. MCF14 caused an increase in the linewidths of the K268$^{6.32}$ and K116$^{3.29}$ major peaks, together with a significant increase in the peak intensity of K268$^{6.32}$ (Figure 3B). As with AVP, the smallest peak of K268$^{6.32}$ was also split in two peaks of unequal intensities but at different chemical shifts from AVP, one being close to the small peak found in the inactive states (*apo* and TVP-bound). Hence, the NMR spectra of V2R in its *apo* and agonist-bound forms indicate at least three different conformations of TM6. Interestingly, three different conformations were observed in the cryo-EM maps of the native receptor complexed with AVP and the Gs protein,[45] suggesting that these conformations may vary in the engagements of the Gs protein and in the capacities of nucleotide exchange, as reported for the adenosine A2A receptor.[44]

Altogether, the MD and NMR data show that TVP, MCF14 and AVP binding had differential impacts on the TM6 intracellular extremity, both conformationally and dynamically, corresponding to their disparate signaling profiles.

Biased activation mechanism revealed by MD simulations. A close inspection of MD simulations illustrated distinct TM7-H8 conformations in V2R-MCF14 compared to V2R-AVP, which are likely associated with the Gs bias (Figure 4). MCF14 bound deeper in the orthosteric pocket and inserted between TM2 and TM7, which altered the conformations of the conserved Na^+-binding site (Figure 5A).

The NP$^{7.50}$xxY motif moved inward and Y325$^{7.53}$ formed water-mediated or direct H-bonds with T134$^{3.47}$ in TM3. H8 exhibited more constrained conformations and was closer to TM1 than in V2R-AVP (Figure 5A). ^{par}MCF14 gave rise to the same phenomenon, despite larger fluctuations in the orthosteric pocket due to lower affinity (Figure S5A and S9). Remarkably, *apo*-V2R^{I130N} showed similar TM7-H8-TM1 conformations to those in V2R-MCF14 on the intracellular side. Similar to V2R-MCF14, these conformations were stabilized by a direct H-bond between Y325$^{7.53}$ of the NP$^{7.50}$xxY motif and the mutated I130$^{3.43}$N residue in TM3 (Figure 5A). The H8-TM1 region was indeed more compact in V2R-MCF14 and *apo*-V2R^{I130N} than in the other system (Figures 5A and S9B). Interestingly, stimulation of V2R^{I130N} by AVP (AVP-V2R^{I130N}) recovered the wt V2R-AVP-like conformations at H8-TM1, despite the H-bonds between th I130$^{3.43}$N and NP$^{7.50}$xxY (Figure 5B). Since the I130$^{3.43}$N variant could recruit βArr2 upon AVP stimulation (Figure 2B and S7), the distinct H8-TM1 conformations in V2R-MCF14 and *apo*-V2R^{I130N} suggest a link to their lack of detectable βArr signaling in the cell assays, clearly differentiable from V2R-AVP and V2R^{I130N}-AVP.

DISCUSSION

Biased signaling has raised a tremendous interest during the last decade, because it holds the promise of more specific drugs with fewer side-effects. This phenomenon may occur via ligand-dependent mechanisms or mutations, many of which alter the conformational equilibrium of GPCRs.

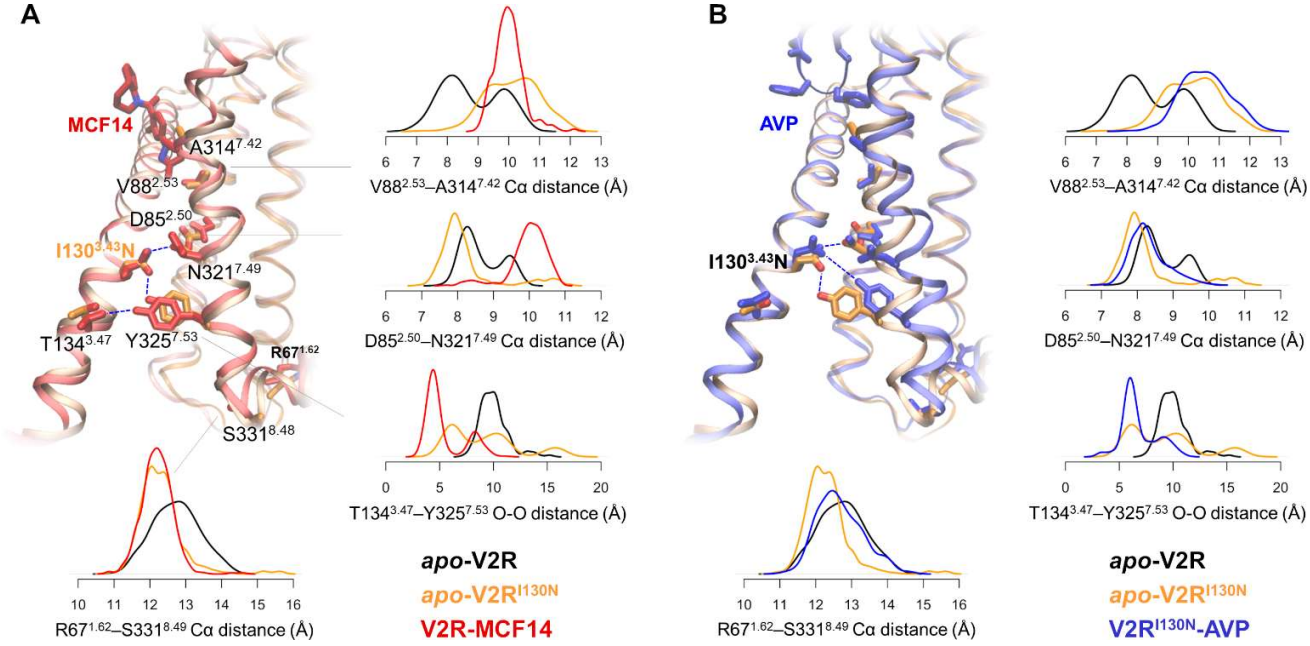

Figure 5. **Conformational changes of TM7 and H8 induced by the mutation I130$^{3.43}$N compared to MCF14 and AVP.** At the ligand- and Na^+-binding sites, *apo*-V2R^{I130N} behaved similarly to V2R^{I130N}-AVP. At the NPxxY motif, the I130$^{3.43}$N mutation generated H-bonds with N321$^{7.49}$ and Y325$^{7.53}$, pulling Y325$^{7.53}$ toward TM3. This led to compactness of H8 and TM1, similar to the effect of MCF14 (**A**). This effect was overridden allosterically by AVP binding to V2R^{I130N} (**B**).

While the TM6 displacement is a known marker for receptor activation, our findings indicate that TM7-H8 conformational changes are likely associated with βArr signaling (Figures 4 and 5). Overall, the 8 simulation systems exhibited differential V2R conformations on the intracellular side that correspond to their signaling profiles (Figures S9A and S10). This is in line with our previous findings using fluorescent probes in V2R TM6 and TM7-H8 junctions,[16] but the present work provides a far more comprehensive mechanistic view. In this work, we elicited a mechanism where distinct conformations of TM7 lead to compactness of H8 toward TM1, which is likely associated with G protein bias (Figure 6). The biased agonist MCF14 triggered these

conformational changes allosterically, through the conserved Na^+-binding site in TM2 and the $NP^{7.50}xxY$ motif in TM7. The $I130^{3.43}N$ mutation, however, acted directly on the $NP^{7.50}xxY$ motif and resulted in similar H8-TM1 conformations to those in V2R-MCF14. In our previous work on the biased mechanism of the μ-opioid receptor, we also observed similar patterns at H8 associated with Gi protein biased agonists.[24]

Residue $I130^{3.43}$ may play a particular role in GPCR activation and biased signaling. It is conserved in 74% of class A GPCRs,[45] and has been shown to be important in constraining the inactive state of several receptors. Namely, its mutations led to constitutive activation of the thyroid-stimulating hormone receptor,[46,47] the β2-adrenergic receptor,[48] the rat M1 muscarinic receptor,[49] the C5A receptor,[50] and the cysteinyl leukotriene receptor 2.[51] A systematic mutational investigation at this position of the melacortin 4 receptor indicated its important role in signaling bias.[52] We show here that the $I130^{3.43}N$ mutation in V2R led to constitutive cAMP signaling without βArr2 recruitment, in line with previous reports. [33] By contrast, upon AVP stimulation, the $V2R^{I130N}$ variant displayed higher βArr2 recruitment level than wt V2R. This indicates a particular role of residue $I130^{3.43}$ in the βArr2 signaling pathway. Moreover, our findings suggest that this position is critical owing to its direct interactions with the $NP^{7.50}xxY$ motif in TM7.

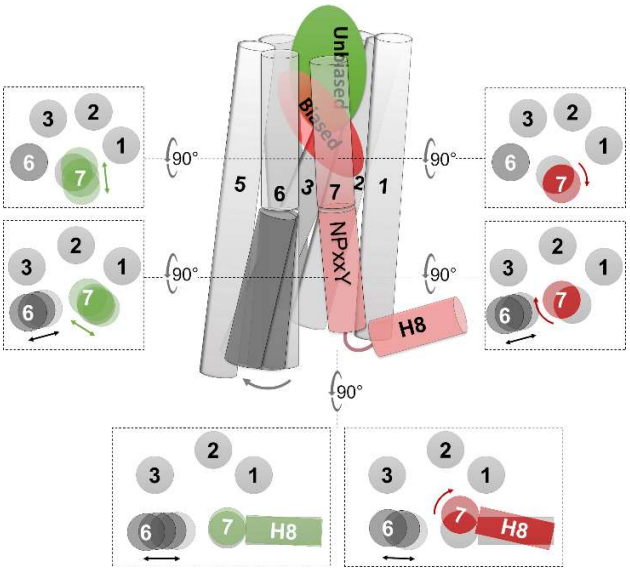

Figure 6. Proposed scheme of V2R conformational changes induced by G protein-biased and unbiased agonists. G protein-biased agonist (red) binds deeper in the orthosteric pocket and induces different TM7 and H8 conformations than unbiased agonist (green). Biased agonist triggers inward movements of TM7-H8 toward TM1 in the intracellular half of V2R, closing the ICL1-H8 gap. Cross-sections of the TMs are viewed from the top (extracellular side). Upon binding, both biased and unbiased agonists induce outward movements of TM6 on the intracellular side.

Increasing evidence points to the particular role of TM7 and H8 in the G protein/β-arrestin bias of class A GPCRs. Some studies attributed ligand bias to specific ligand-TM7 interactions,[53–55] others associated biased signaling to distinct conformations in the Na^+-binding site, the $NP^{7.50}xxY$ motif, as well as H8.[13,14,16,17,21,55–61] H8 conformations may directly affect βArr coupling or trigger long-range effects on the receptor C-terminus involved in βArr activation. Indeed, a recent study on the β2 adrenergic receptor shows that βArr activation requires synergy between receptor agonism and the C-terminus phosphorylation.[62] These studies suggest overall conserved mechanisms associated with biased activation of class A GPCRs (Figure 6). However, the detailed structural features may vary among different receptors, ligands and mutants.

Clinical translation of GPCR ligand bias is very challenging due to the complexity of GPCR signaling, as well as the difficulties in assaying the bias in cells and disease models. In addition to the receptor conformational heterogeneity, many other factors are involved in biased signaling that are so far poorly understood, e.g. kinetics of ligand binding, allosteric communications with G protein/βArr binding and activation, receptor phosphorylation patterns, compartmentalized signaling, receptor polymorphism and local environment, *etc*.[4] Nevertheless, structural analysis of receptor-ligand interactions and bias-associated receptor conformations can provide direct information for structure-based design of biased ligands.[21,53,54,57,63] The approach of combining ligand paramagnetic tagging with enhanced-sampling MD simulations offers a solution to the common challenge of determining ligand binding poses. The diverse V2R conformations obtained in this work will enable virtual screening and rational design of V2R ligands with different signaling profiles. Our findings also indicate conserved structural patterns for G protein bias that may be common to other class A GPCRs.

METHODS

V2R construction and expression. The V2R construct used for NMR analysis was already described.[36] Briefly, the *Spodoptera frugiperda (Sf9)*-optimized sequence of the human V2R was cloned into a pFastBac™1 vector (Invitrogen) using EcoR1/Xba1 restriction sites. To facilitate expression and purification of the V2R construct, the hemagglutinin signal peptide (MKTIIALSYIFCLVFA) followed by a Flag tag (DYKDDDDA) were added at the N-terminus, and a Twin-strep-tag® (WSHPQFEKGGGSGGGSGGGSWSHPQFEK) inserted at the C-terminus. In addition, N22 was substituted with a glutamine residue to avoid N-glycosylation, and C358 mutated into an alanine to eliminate potential intermolecular disulfide bridges during solubilization and purification. A Tobacco Etch Virus (TEV) protease cleavage site (ENLYFQG - following the Flag tag) and 2 Human Rhinovirus 3C protease (3C) cleavage sites (LEVLFQGP - 1 inserted in the N-terminus between D30 and T31, the other inserted in the C-terminus between G345 and Q354 and replacing R346-TPPSLG-P353) were also added to remove N and C termini and facilitate NMR analysis (Figure S1). M1L2 residues were replaced by AS residues, and LE residues were added before the Twin-strep-tag®, during subcloning (introduction of Nhe1 and Xho1 restriction sites, respectively). Sequence modifications did not affect the receptor ligand binding or function.[36] The V2R was expressed in Sf9 insect cells using the Bac-to-Bac® baculovirus expression system (Invitrogen) according to manufacturer's instructions. Insect cells were grown in suspension in EX-CELL® 420 medium (Sigma-Aldrich) to a density of 4×10^6 cells per ml and infected with the recombinant baculovirus encoding V2R at a multiplicity of infection of 2 to 3. The culture medium was supplemented with the specific V2R pharmacochaperone antagonist Tolvaptan (Sigma-Aldrich) at 1 μM to allow proper folding and membrane targeting of the receptor.[31,64] The cells were infected for 48 h to 54 h at 28 °C. Before harvesting, the expression of the V2R was controlled by immunofluorescence using an anti-Flag M1 antibody coupled to an Alexa488 fluorophore. Cells were then harvested by centrifugation (2 steps, 15 min then 20 min at 3,000g) and the cell pellets were stored at -80 °C until use.

The different mutants of the V2R (K100R, K116R, K268R) were all derived from the matrix described above using the gene synthesis and molecular biology services of Eurofins Genomics.

V2R purification and labeling. After thawing the frozen cell pellets, cells were lysed by osmotic shock in 10 mM Tris-HCl pH 8, 1 mM EDTA buffer containing 2 $mg.ml^{-1}$ iodoacetamide (Sigma-Aldrich), Tolvaptan 1 µM and protease inhibitors [leupeptine (5 $\mu g.ml^{-1}$) (Euromedex), benzamidine (10 $\mu g.ml^{-1}$) (Sigma-Aldrich), and phenylmethylsulfonyl fluoride (PMSF) (10 $\mu g.ml^{-1}$) (Euromedex)]. Lysed cells were centrifuged (15 min at 38,400g) and the pellets containing crude membranes were solubilized using a glass dounce tissue grinder (15 + 20 strokes using A and B pestles respectively) in a solubilization buffer containing 20 mM Tris-HCl pH 8, 500 mM NaCl, 0.5 % (w/v) n-dodecyl-β-D-maltopyranoside (DDM, Anatrace), 0.2 % (w/v) sodium cholate (Sigma-Aldrich), 0.03 % (w/v) cholesteryl hemisuccinate (CHS, Sigma-Aldrich), 20 % Glycerol (VWR), 2 $mg.ml^{-1}$ iodoacetamide, 0.75 $ml.L^{-1}$ Biotin Biolock (IBA), Tolvaptan 1 µM and protease inhibitors. The extraction mixture was stirred for 1 h at 4 °C and centrifuged (20 min at 38,400g).

The cleared supernatant was poured onto equilibrated Strep-Tactin resin (IBA) for a first affinity purification step. After 2 h of incubation at 4 °C under stirring, the resin was laid down into a column and washed three times with 10 column volume (CV) of a buffer containing 20 mM Tris-HCl pH 8, 500 mM NaCl, 0.1 % (w/v) DDM, 0.02 % (w/v) sodium cholate, 0.03 % (w/v) CHS, Tolvaptan 1 µM. The bound receptor was eluted in the same buffer supplemented with 2.5 mM Desthiobiotin (IBA). The amount of V2R was calculated by UV absorbance spectroscopy.

The eluate supplemented with 2 mM $CaCl_2$ was loaded onto an M1 anti-Flag affinity resin (Sigma-Aldrich) for a second affinity purification. After loading, the DDM detergent was then gradually exchanged into a buffer with Lauryl Maltose Neopentyl glycol (LMNG, Anatrace) (20 mM HEPES pH 7.4, 100 mM NaCl, 0.01 % CHS and 0.5 % LMNG). The LMNG concentration was then decreased from 0.5 % to 0.02 %. The V2R was then eluted in 20 mM HEPES pH 7.4, 100 mM NaCl, 0.02 % LMNG, 0.002 % CHS, 2 mM EDTA, 10 µM Tolvaptan and 0.2 $mg.ml^{-1}$ Flag peptide (Covalab). The amount of V2R was estimated by UV absorbance spectroscopy and was then cleaved overnight using the HRV3C protease at a 1:20 weight ratio (HRV3C:V2R) at 4 °C. Concomitantly, the V2R was labeled onto its lysine residues by reductive methylation using 10 mM ^{13}C-formaldehyde (Sigma-Aldrich) in the presence of 10 mM sodium cyanoborohydride (Sigma-Aldrich) following the protocol described previously.[40,41]

The 3C-cleaved ^{13}C-dimethyl-lysine-labeled V2R was concentrated using 50-kDa concentrators (Millipore) and separated from the protease using a Superdex 200 10/300 column on an AKTA purifier system (0.5 mL/min flowrate, buffer 20 mM HEPES pH 7.4, 100 mM NaCl, 0.02 %, no ligand). Fractions corresponding to the pure monomeric V2R were pooled and dialyzed first 2 h at 4 °C using a 3-kDa MWCO cassette in 20 mM HEPES pH 7.4, 40 mM NaCl, 0.02 % LMNG, 0.002 % CHS. Then, the sample was dialyzed again 2 h at 4 °C in 98.85 % D_2O buffer with 20 mM HEPES-d18 pH 7.4 (uncorrected), 40 mM NaCl, 0.02 % LMNG, 0.002 % CHS. V2R was then concentrated using a 50-kDa MWCO concentrator up to 250 µl, and then diluted with 2 ml of 98.85 % D_2O buffer with 20 mM HEPES-d18 pH 7.4, 40 mM NaCl before a second concentration step. The final concentration of V2R was 25-30 µM in buffer containing 20 mM HEPES-d18 pH 7.4, 40 mM NaCl, 0.0022 % LMNG and 0.0002 % CHS (NMR buffer). Acid 4,4-dimethyl-4-silapentane-1-sulfonique (DSS) was added at a final concentration of 100 µM as a standard to calibrate the NMR analysis.

NMR spectroscopy. Final samples (~270 µl at 30-35µM) were loaded into Shigemi microtubes whose susceptibility matched with D_2O. All data for ligands and mutant studies were acquired on 700 MHz Bruker Avance III spectrometers (Bruker, Rheinstetten, Germany), equipped with 5 mm cryogenic H/C/N/D probes with z axis gradient at 293K, unless otherwise specified. ^{1}H-^{13}C correlation spectra were recorded using heteronuclear multiple-quantum coherence (HMQC) experiments in echo anti-echo mode. Spectral widths in ω1 and ω2 were 8,417.5 Hz and 3,518.6 Hz at 700 MHz centred at 40 p.p.m. ^{13}C decoupling was performed with a GARP4 sequence. Thirty-two steady-state scans preceded data acquisition. Typically, 134 complex points with per FID were recorded, to ensure a 27-Hz resolution per point at 700 MHz before zero filling, with 32 scans and a relaxation delay of 1.5 s (^{par}dLVP, ^{par} MCF14) or 80 scans and a relaxation delay of 0.5 s (AVP, MCF14, TVP). Total collection time varied between 3 and 4 h, depending on the sample concentration. Ligands were dissolved in NMR buffer (AVP, ^{par}dLVP) or in perdeuterated dimethyl d6-sulfoxide (d6-DMSO, Cambridge Isotope) (MCF14, ^{par}MCF14, TVP) to 10 mM and directly added to the sample in the Shigemi tube at a final concentration five (AVP, MCF14) or 0.95 fold (^{par}dLVP, ^{par}MCF14) of receptor. The non-paramagnetic agonists (AVP, MCF14, TVP) have high affinities for µOR (< 0.1 µM). At saturating concentrations (30 µM and 150 µM for V2R and non-paramagnetic ligands, respectively), according to the law of mass action, 99% of the V2R should be in complex at 10 µM concentration of agonists (~100 times the Kd concentration). The effect of paramagnetic ligands was studied using sub-stoichiometric ligand concentrations, to promote binding in the receptor orthosteric site. Reduction was achieved by the addition of 5 equivalents of freshly prepared ascorbic acid dissolved at 10 mM in the NMR buffer.

All NMR spectra were processed using the suite of programs provided in the NMRPipe/NMRDraw software distribution.[65] The spectra were normalized using DSS (2,2-dimethyl-2-silapentane-5-sulfonic acid) as an internal reference. For peak fitting analysis, spectra were processed with a squared sine-bell window function in each dimension, and zero-filled to 4096 x 1024 data points in time domain data t2 and t1, respectively. Spectra were fit with the program nlinLS, provided as a part of nmrDraw package. Gaussian models were used for the fitting in each dimension, starting from values obtained from the peak-peaking routine in nmrDraw. The quality of the fits was examined visually by estimating the residual difference between the experimental data and the results of the model calculations. Peak intensity of the ^{13}C-dimethylated lysines were normalized to the intensity of the G52 (cleaved N terminus) and buffer peaks. Errors in the peak volume were calculated based on the effect of random noise for the peak height estimated by nlinLS (TVP) or by du-(tri-)plicating experiments starting purification of new V2R culture batches (AVP, ^{par}AVP, MCF14, ^{par}MCF14). Figures were drawn with the Topspin 3.6 (Bruker, Inc) and NMRview packages.[66]

Time-resolved Fluorescence Resonance Energy Transfer binding assays. V2R binding studies using Tag-Lite assays (PerkinElmer Cisbio) based on time-resolved fluorescence resonance energy transfer (TR-FRET) measurements were previously described.[36,67,68] Briefly, HEK cells were plated (15,000 per well) in precoated with poly-L-ornithine (14 µg/ml, Sigma-Aldrich) white-walled, flat-bottom, 96-well plates (Greiner CELLSTAR plate, Sigma-Aldrich) in Dulbecco's minimum essential medium

(DMEM) containing 10 % fetal bovine serum (FBS, Eurobio), 1 % nonessential amino acids (GIBCO), and penicillin/streptomycin (GIBCO). Cells were transfected 24 h later with a plasmid coding for the 3C-cleaved V2R version used in NMR studies (Figure S1A) fused at its N-terminus to the enzyme-based self-labeling SNAP-tag (pRK5-SNAP vector, PerkinElmer Cisbio). The I130N mutation was introduced in this V2R construction (Figure S1A). Transfections were performed with X-tremeGENE 360 (Merck), according to the manufacturer's recommendations: 10 µl of a premix containing DMEM, X-tremeGENE 360 (0.3 µl per well), SNAP-V2 coding plasmid (30 ng per well, whatever the construct used), and noncoding plasmid (70 ng per well) were added to the culture medium. After a 48-hour culture period, cells were rinsed once with Tag-lite medium (PerkinElmer Cisbio) and incubated in the presence of Tag-lite medium containing 100 nM benzylguanine-Lumi4-Tb for at least 60 min at 37 °C. Cells were then washed four times. For saturation studies, cells were incubated for at least 4 h at 4 °C in the presence of benzazepine-red nonpeptide vasopressin antagonist (BZ-DY647, PerkinElmer Cisbio) at various concentrations ranging from 10^{-10} to 10^{-7} M. Nonspecific binding was determined in the presence of 10 µM vasopressin. For competition studies, cells were incubated for at least 4 h at 4 °C with benzazepine-red ligand (5 nM) and increasing concentrations of vasopressin ranging from 10^{-12} to 10^{-5} M. Fluorescent signals were measured at 620 nm (fluorescence of the donor) and at 665 nM (FRET signal) on a PHERAstar (BMG LABTECH). Results were expressed as the 665/620 ratio [10,000 × (665/620)]. A specific variation of the FRET ratio was plotted as a function of benzazepine-red concentration (saturation experiments) or competitor concentration (competition experiment). All binding data were analyzed with GraphPad 9.1.1 (GraphPad Prism Software Inc.) using the one site-specific binding equation. All results are expressed as the means ± SEM of at least three independent experiments performed in triplicate. K_i values were calculated from median inhibitory concentration values with the Cheng-Prusoff equation.

cAMP accumulation assays. V2R (WT and mutants K100R, I130N) functional studies based on TR-FRET measurements were described previously.[31,36,69] Briefly, HEK cells were plated in pre-coated black-walled 96-well plates (Falcon) at 5,000 cells per well, and then transfected 24 h later with a plasmid coding for the SNAP-tagged V2R version used in NMR studies. Transfections were performed with X-tremeGENE 360 (Merck), according to the manufacturer's recommendations: 10 µl of a premix containing DMEM, X-tremeGENE 360 (0.3 µl per well), pRK5-SNAP-V2R coding plasmid (ranging from 0.3 to 30 ng per well, depending on the V2R construct), and pRK5 noncoding plasmid (ranging from 70 to 99.7 ng per well) were added to the culture medium. After a 24-hour culture period, cells were treated for 30 min at 37 °C in the cAMP buffer with or without increasing ligands concentrations (10^{-12} to 3.16×10^{-5} M) in the presence of 0.1 mM RO201724, a phosphodiesterase inhibitor (Sigma-Aldrich). The accumulated cAMP was quantified using the cAMP Dynamic 2 Kit (PerkinElmer Cisbio) according to the manufacturer's protocol. Fluorescent signals were measured at 620 and 665 nm on a PHERAstar microplate reader. Data were plotted as the FRET ratio [10,000 × (665/620)] as a function of AVP concentration [log (AVP)]. Data were analyzed with GraphPad Prism v 9.1.1 (GraphPad Prism Software Inc.) using the "dose-response stimulation" subroutine. Median effective concentrations were determined using the log(agonist) versus response variable slope (four parameters) fit procedure. Experiments were repeated at least three times on different cultures, each condition in triplicate. Data are presented as means ± SEM.

β-arrestin2 recruitment assays. The recruitment assay of βArr2 was previously described.[39] Briefly, upon GPCR activation, βArrs are recruited to stop G protein signaling and to initiate clathrin-mediated receptor internalization. During this process, the release of the C-terminal domain of βArrs is associated with the binding of βArrs to the adaptor protein 2 (AP2). This interaction can be measured using the HTRF® technology (PerkinElmer CisBio) based on the use of two specific antibodies, one directed against βArr2, the second one specific for AP2. In this assay (βArr2 recruitment kit, PerkinElmer CisBio), the AP2 antibody is labeled with a Europium (Eu) cryptate fluorescent donor, and the one against βArr2 is labeled with a d2 fluorescent acceptor, their proximity being detected by FRET signals. The specific signal is positively modulated in proportion with the recruitment of βArr2 to AP2 upon V2R activation by AVP. Briefly, HEK cells were plated at a seeding density of 25,000 cells per well in a precoated white-walled 96-well plates (CELLSTAR plate, Sigma-Aldrich) for 24 h, in DMEM complemented with 10 % FBS, 1 % non-essential amino acids, and 1 % penicillin-streptomycin antibiotics solution. To produce the V2R, the cells were transfected with a pRK5-SNAP-V2R plasmid (from 0.6 to 30 ng per well, depending on the construct, wt or I130N NMR versions) using X-tremeGENE 360 (Merck), according to the manufacturer's recommendations. After a 24-hour culture, cells were used to evaluate the recruitment of βArr2 to AP2 upon V2R activation with the βArr2 recruitment kit (PerkinElmer CisBio) following the manufacturer recommendation. Briefly, the cells were first washed one time with DMEM-free and incubated 2 h at room temperature (RT) with 100 µl per well of stimulation buffer containing various concentrations of the different ligands (ranging from 10^{-12} M to 10^{-5} M). The medium was then replaced by 30 µl per well of stabilization buffer for 15 min at RT. The cells were then washed three times with 100 µl per well of wash buffer before adding 100 µl per well of a pre-mix of Eu cryptate and d2 antibodies in detection buffer. Following overnight incubation at RT, 80 µl of medium was removed from each well before reading the 96-well plates a PHERAstar by measuring the signals of the donor (Eu cryptate-labeled AP2 antibody) at a wavelength of 620 nm, and of the acceptor at 665 nm (d2-labeled βArr2). Finally, the results were expressed as the FRET ratio [(665/620) x 10,000] and plotted using GraphPad 9.1.1 (GraphPad Prism software inc.). Experiments were repeated at least three times on different cultures, each condition in triplicate. Data are presented as means ± SEM.

Molecular Dynamic simulations. The initial models of V2R in inactive state were built using Modeller v9.15 based on the cryo-EM structures of AVP-V2R-Gs (PDBs 7dw9 [37] and 7BB6 [36]) and the X-ray crystal structure of the oxytocin receptor in inactive state (PDB 6TPK[70]). PACKMOL-Memgen[71] was used to assign the side-chain protonation states and embed the models in a lipid bilayer of POPC and cholesterol in 3:1 ratio. The systems were solvated in a periodic 78 × 78 × 112 $Å^3$ box of explicit water and neutralized with 0.15 M of Na^+ and Cl^- ions. We used the Amber ff14SB,[72] GAFF[73] and lipid14[74] force fields, and the TIP3P water models[75] and the Joung-Cheatham ion parameters[76]. Effective point charges of the ligands were obtained by RESP fitting[77] of the electrostatic potentials calculated with the HF/6-31G* basis set. After energy minimization, all-atom MD simulations were carried out using Gromacs 5.1[78] patched with the PLUMED 2.3 plugin.[79] Each system was gradually heated to 310 K and pre-equilibrated during 10 ns of brute-force MD in the *NPT*-ensemble. The replica exchange with solute scaling (REST2)[80] technique was used to enhance the MD sampling (see Supplementary Methods for details). We performed 60 ns × 64 replicas of REST2 MD in the *NVT* ensemble for each system. The first 20 ns were discarded for

equilibration. The trajectories of the original unmodified replica were collected and analyzed.

ASSOCIATED CONTENT

Supporting Information. The supporting material is available free of charge via the Internet at http://pubs.acs.org.
Experimental details, Figures S1-S10 and Table S1-S2 (PDF).

AUTHOR INFORMATION

Corresponding Author

* Helene.Demene@cbs.cnrs.fr or Bernard.Mouillac@igf.cnrs.fr or Xiaojing.Cong@igf.cnrs.fr

Present Addresses

†AB Science, Paris 75008, France

Author Contributions

The manuscript was written through contributions of all authors. All authors have given approval to the final version of the manuscript.

Funding Sources

This work was supported in part by grants from FRM (DEQ20150331736), and ANR (19-CE11-0014-1). This work was also supported by the University of Strasbourg, the Interdisciplinary Thematic Institute IMS (ANR-10-IDEX-0002) and SFRI (STRAT'US project, ANR-20-SFRI-0012) under the framework of the French Investments for the Future Program. Core funding were provided by CNRS, INSERM and Université de Montpellier. MD simulations were performed using HPC resources from GENCI-TGCC (grant 2021-2022 A0100712461).

Notes

The authors declare no competing interests.

ACKNOWLEDGMENT

The CBS is a member of the French Infrastructure for Integrated Structural Biology (FRISBI), supported by the National Research Agency (ANR-10-INBS-05) and is a GIS-IBIsA platform. We also thank the Institut de Génomique Fonctionnelle Arpege Pharmacology (http://www.arpege.cnrs.fr) platform for access to their instruments, and Perkin Elmer CisBio for providing reagents.

ABBREVIATIONS

AP2, adaptor protein 2; AVP, Arginine-Vasopressin; βArr, β-arrestin; cNDI, congenital nephrogenic diabetes insipidus; cryo-EM, cryogenic electron microscopy; dLVP, deaminated lysine vasopressin; GPCR, G protein-coupled receptor; H8, helix 8; H-bond, hydrogen bond; HMQC, Heteronuclear Multi Quanta Coherence; LVP, lysine-vasopressin;MD, molecular dynamics; NMR, Nuclear Magnetic Resonance; NSIAD, nephrogenic syndrome of inappropriate antidiuresi ; ^{par}dLVP, paramagnetically tagged dLVP; ^{par}MCF14, paramagnetically tagged MCF14; PRE, paramagnetic relaxation enhancements; REST2, replica exchange TR-FRET, time-resolved fluorescence resonance energy transfer; with solute scaling; wt, wild-type; TM, Transmembrane helix; TVP, Tolvaptan; V2R, vasopressin type 2 receptor;

REFERENCES

(1) Santos, R.; Ursu, O.; Gaulton, A.; Bento, A. P.; Donadi, R. S.; Bologa, C. G.; Karlsson, A.; Al-Lazikani, B.; Hersey, A.; Oprea, T. I.; Overington, J. P. A Comprehensive Map of Molecular Drug Targets. *Nat. Rev. Drug Discov.* **2017**, *16* (1), 19–34. https://doi.org/10.1038/NRD.2016.230.

(2) Hauser, A. S.; Attwood, M. M.; Rask-Andersen, M.; Schioth, H. B.; Gloriam, D. E. Trends in GPCR Drug Discovery: New Agents, Targets and Indications. *Nat Rev Drug Discov* **2017**, *16* (12), 829–842.

(3) Wootten, D.; Christopoulos, A.; Marti-Solano, M.; Babu, M. M.; Sexton, P. M. Mechanisms of Signalling and Biased Agonism in G Protein-Coupled Receptors. *Nat Rev Mol Cell Biol* **2018**, *19* (10), 638–653.

(4) Kolb, P.; Kenakin, T.; Alexander, S. P. H.; Bermudez, M.; Bohn, L. M.; Breinholt, C. S.; Bouvier, M.; Hill, S. J.; Kostenis, E.; Martemyanov, K. A.; Neubig, R. R.; Onaran, H. O.; Rajagopal, S.; Roth, B. L.; Selent, J.; Shukla, A. K.; Sommer, M. E.; Gloriam, D. E. Community Guidelines for GPCR Ligand Bias: IUPHAR Review 32. *British Journal of Pharmacology*. 2022. https://doi.org/10.1111/bph.15811.

(5) Tao, Y. X. Constitutive Activation of G Protein-Coupled Receptors and Diseases: Insights into Mechanisms of Activation and Therapeutics. *Pharmacol. Ther.* **2008**, *120* (2), 129–148. https://doi.org/10.1016/J.PHARMTHERA.2008.07.005.

(6) Yang, L. K.; Hou, Z. S.; Tao, Y. X. Biased Signaling in Naturally Occurring Mutations of G Protein-Coupled Receptors Associated with Diverse Human Diseases. *Biochim. Biophys. Acta - Mol. Basis Dis.* **2021**, *1867* (1), 165973. https://doi.org/10.1016/j.bbadis.2020.165973.

(7) Venkatakrishnan, A. J.; Deupi, X.; Lebon, G.; Heydenreich, F. M.; Flock, T.; Miljus, T.; Balaji, S.; Bouvier, M.; Veprintsev, D. B.; Tate, C. G.; Schertler, G. F. X.; Babu, M. M. Diverse Activation Pathways in Class A GPCRs Converge near the G-Protein-Coupling Region. *Nat. Publ. Gr.* **2016**, *536* (7617), 484–487. https://doi.org/10.1038/nature19107.

(8) Zhou, Q.; Yang, D.; Wu, M.; Guo, Y.; Guo, W.; Zhong, L.; Cai, X.; Dai, A.; Jang, W.; Shakhnovich, E.; Liu, Z. J.; Stevens, R. C.; Lambert, N. A.; Babu, M. M.; Wang, M. W.; Zhao, S. Common Activation Mechanism of Class a GPCRs. *Elife* **2019**, *8*, 1–31. https://doi.org/10.7554/eLife.50279.

(9) Weis, W. I.; Kobilka, B. K. The Molecular Basis of G Protein–Coupled Receptor Activation. *Annu. Rev. Biochem.* **2018**, *87*, 897. https://doi.org/10.1146/ANNUREV-BIOCHEM-060614-033910.

(10) Rasmussen, S. G.; Choi, H. J.; Fung, J. J.; Pardon, E.; Casarosa, P.; Chae, P. S.; Devree, B. T.; Rosenbaum, D. M.; Thian, F. S.; Kobilka, T. S.; Schnapp, A.; Konetzki, I.; Sunahara, R. K.; Gellman, S. H.; Pautsch, A.; Steyaert, J.; Weis, W. I.; Kobilka, B. K. Structure of a Nanobody-Stabilized Active State of the Beta(2) Adrenoceptor. *Nature* **2011**, *469* (7329), 175–180.

(11) Rasmussen, S. G.; DeVree, B. T.; Zou, Y.; Kruse, A. C.; Chung, K. Y.; Kobilka, T. S.; Thian, F. S.; Chae, P. S.; Pardon, E.; Calinski, D.; Mathiesen, J. M.; Shah, S. T.; Lyons, J. A.; Caffrey, M.; Gellman, S. H.; Steyaert, J.; Skiniotis, G.; Weis, W. I.; Sunahara, R. K.; Kobilka, B. K. Crystal Structure of the Beta2 Adrenergic Receptor-Gs Protein Complex. *Nature* **2011**, *477* (7366), 549–555.

(12) Ballesteros, J. A.; Weinstein, H. Integrated Methods for the Construction of Three-Dimensional Models and Computational Probing of Structure-Function Relations in G Protein-Coupled Receptors. *Methods Neurosci.* **1995**, *25* (C), 366–428. https://doi.org/10.1016/S1043-9471(05)80049-7.

(13) Lamichhane, R.; Liu, J. J.; White, K. L.; Katritch, V.; Stevens, R. C.; Wüthrich, K.; Millar, D. P. Biased Signaling of the G-Protein-Coupled Receptor B2AR Is Governed by Conformational Exchange Kinetics. *Structure* **2020**, *28* (3), 371-377.e3. https://doi.org/10.1016/j.str.2020.01.001.

(14) Liu, J. J.; Horst, R.; Katritch, V.; Stevens, R. C.; Wuthrich, K. Biased Signaling Pathways in Beta2-Adrenergic Receptor Characterized by 19F-NMR. *Science (80-.).* **2012**, *335* (6072), 1106–1110.

(15) Louet, M.; Casiraghi, M.; Damian, M.; Costa, M. G.; Renault, P.; Gomes, A. A.; Batista, P. R.; M'Kadmi, C.; Mary, S.; Cantel, S.; Denoyelle, S.; Ben Haj Salah, K.; Perahia, D.; Bisch, P. M.; Fehrentz, J. A.; Catoire, L. J.; Floquet, N.; Banères, J. L. Concerted Conformational Dynamics and Water Movements in the Ghrelin G Protein-Coupled Receptor. *Elife* **2021**, *10*. https://doi.org/10.7554/ELIFE.63201.

(16) Rahmeh, R.; Damian, M.; Cottet, M.; Orcel, H.; Mendre, C.; Durroux, T. Structural Insights into Biased G Protein-Coupled Receptor Signaling Revealed by Fl Uorescence Spectroscopy. **2012**, *14* (17). https://doi.org/10.1073/pnas.1201093109.

(17) Cong, X.; Maurel, D.; Déméné, H. H.; Vasiliauskaité-brooks, I.; Hagelberger, J.; Peysson, F.; Saint-Paul, J.; Golebiowski, J.; Granier, S.; Sounier, R. Molecular Insights into the μ -Opioid Receptor Selective Signaling. *Mol. Cell* **2021**, *81* (20), 1–21. https://doi.org/10.1016/J.MOLCEL.2021.07.033.

(18) Okude, J.; Ueda, T.; Kofuku, Y.; Sato, M.; Nobuyama, N.; Kondo, K.; Shiraishi, Y.; Mizumura, T.; Onishi, K.; Natsume, M.; Maeda, M.; Tsujishita, H.; Kuranaga, T.; Inoue, M.; Shimada, I. Identification of a Conformational Equilibrium That Determines the Efficacy and Functional Selectivity of the m -Opioid Receptor Angewandte. **2015**. https://doi.org/10.1002/ange.201508794.

(19) Wingler, L. M.; Elgeti, M.; Hilger, D.; Latorraca, N. R.; Lerch, M. T.; Staus, D. P.; Dror, R. O.; Kobilka, B. K.; Hubbell, W. L.; Lefkowitz, R. J. Angiotensin Analogs with Divergent Bias Stabilize Distinct Receptor Conformations. *Cell* **2019**, *176* (3), 468-478.e11. https://doi.org/10.1016/j.cell.2018.12.005.

(20) Xu, J.; Hu, Y.; Kaindl, J.; Risel, P.; Hübner, H.; Maeda, S.; Niu, X.; Li, H.; Gmeiner, P.; Jin, C.; Kobilka, B. K. Conformational Complexity and Dynamics in a Muscarinic Receptor Revealed by NMR Spectroscopy. *Mol. Cell* **2019**, *75* (1), 53-65.e7. https://doi.org/10.1016/j.molcel.2019.04.028.

(21) Suomivuori, C. M.; Latorraca, N. R.; Wingler, L. M.; Eismann, S.; King, M. C.; Kleinhenz, A. L. W.; Skiba, M. A.; Staus, D. P.; Kruse, A. C.; Lefkowitz, R. J.; Dror, R. O. Molecular Mechanism of Biased Signaling in a Prototypical G Protein-Coupled Receptor. *Science* **2020**, *367* (6480), 881–887. https://doi.org/10.1126/SCIENCE.AAZ0326.

(22) Xu, Z.; Ikuta, T.; Kawakami, K.; Kise, R.; Qian, Y.; Xia, R.; Sun, M. X.; Zhang, A.; Guo, C.; Cai, X. H.; Huang, Z.; Inoue, A.; He, Y. Structural Basis of Sphingosine-1-Phosphate Receptor 1 Activation and Biased Agonism. *Nat. Chem. Biol.* **2022**, *18* (3), 281–288. https://doi.org/10.1038/S41589-021-00930-3.

(23) Zheng, K.; Smith, J. S.; Eiger, D. S.; Warman, A.; Choi, I.; Honeycutt, C. C.; Boldizsar, N.; Gundry, J. N.; Pack, T. F.; Inoue, A.; Caron, M. G.; Rajagopal, S. Biased Agonists of the Chemokine Receptor CXCR3 Differentially Signal through Gα i:β-Arrestin Complexes. *Sci. Signal.* **2022**, *15* (726). https://doi.org/10.1126/SCISIGNAL.ABG5203.

(24) Robben, J. H.; Knoers, N. V. A. M.; Deen, P. M. T. Regulation of the Vasopressin V2 Receptor by Vasopressin in Polarized Renal Collecting Duct Cells. *Mol. Biol. Cell* **2004**, *15* (12), 5693–5699. https://doi.org/10.1091/MBC.E04-04-0337.

(25) Ren, X.; Reiter, E.; Ahn, S.; Kim, J.; Chen, W.; Lefkowitz, R. J. Different G Protein-Coupled Receptor Kinases Govern G Protein and -Arrestin-Mediated Signaling of V2 Vasopressin Receptor. **2005**, 1–6.

(26) Alonso, G.; Galibert, E.; Boulay, V.; Guillou, A.; Jean, A.; Compan, V.; Guillon, G. Sustained Elevated Levels of Circulating Vasopressin Selectively Stimulate the Proliferation of Kidney Tubular Cells via the Activation of V2 Receptors. *Endocrinology* **2009**, *150* (1), 239–250. https://doi.org/10.1210/EN.2008-0068.

(27) Ball, S. G. Vasopressin and Disorders of Water Balance: The Physiology and Pathophysiology of Vasopressin. *Ann. Clin. Biochem.* **2007**, *44* (Pt 5), 417–431. https://doi.org/10.1258/000456307781646030.

(28) Morello, J. P.; Bichet, D. G. Nephrogenic Diabetes Insipidus. *Annu. Rev. Physiol.* **2001**, *63*, 607–630. https://doi.org/10.1146/ANNUREV.PHYSIOL.63.1.607.

(29) Bockenhauer, D.; Bichet, D. G. Pathophysiology, Diagnosis and Management of Nephrogenic Diabetes Insipidus. *Nat. Rev. Nephrol.* **2015**, *11* (10), 576–588. https://doi.org/10.1038/NRNEPH.2015.89.

(30) Mouillac, B.; Mendre, C. Pharmacological Chaperones as Potential Therapeutic Strategies for Misfolded Mutant Vasopressin Receptors; 2017; pp 63–83. https://doi.org/10.1007/164_2017_50.

(31) Jean-Alphonse, F.; Perkovska, S.; Frantz, M.-C.; Durroux, T.; Mejean, C.; Morin, D.; Loison, S.; Bonnet, D.; Hibert, M.; Mouillac, B.; Mendre, C. Biased Agonist Pharmacochaperones of the AVP V2 Receptor May Treat Congenital Nephrogenic Diabetes Insipidus. *J. Am. Soc. Nephrol.* **2009**, *20* (10), 2190–2203. https://doi.org/10.1681/ASN.2008121289.

(32) Rosenthal, S. S.; Feldman, B. J.; Vargas, G. A.; Gitelman, S. E. Nephrogenic Syndrome of Inappropriate Antidiuresis (NSIAD): A Paradigm for Activating Mutations Causing Endocrine Dysfunction. *Pediatr Endocrinol Rv* **2006**, *Suppl. 1*, 66–70.

(33) Erdélyi, L. S.; Mann, W. A.; Morris-Rosendahl, D. J.; Groß, U.; Nagel, M.; Várnai, P.; Balla, A.; Hunyady, L. Mutation in the V2 Vasopressin Receptor Gene, AVPR2, Causes Nephrogenic Syndrome of Inappropriate Diuresis. *Kidney Int.* **2015**, *88* (5), 1070–1078. https://doi.org/10.1038/KI.2015.181.

(34) Tiulpakov, A.; White, C. W.; Abhayawardana, R. S.; See, H. B.; Chan, A. S.; Seeber, R. M.; Heng, J. I.; Dedov, I.; Pavlos, N. J.; Pfleger, K. D. G. Mutations of Vasopressin Receptor 2 Including Novel L312S Have Differential Effects on Trafficking. *Mol. Endocrinol.* **2016**, *30* (8), 889–904. https://doi.org/10.1210/ME.2016-1002/SUPPL_FILE/ME-16-1002.PDF.

(35) Vezzi, V.; Ambrosio, C.; Grò, M. C.; Molinari, P.; Süral, G.; Costa, T.; Onaran, H. O.; Cotecchia, S. Vasopressin Receptor 2 Mutations in the Nephrogenic Syndrome of Inappropriate Antidiuresis Show Different Mechanisms of Constitutive Activation for G Protein Coupled Receptors. *Sci. Rep.* **2020**, *10* (1). https://doi.org/10.1038/S41598-020-65996-W.

(36) Bous, J.; Orcel, H.; Floquet, N.; Leyrat, C.; Lai-Kee-Him, J.; Gaibelet, G.; Ancelin, A.; Saint-Paul, J.; Trapani, S.; Louet, M.; Sounier, R.; Déméné, H.; Granier, S.; Bron, P.; Mouillac, B. Cryo-Electron Microscopy Structure of the Antidiuretic Hormone Arginine-Vasopressin V2 Receptor Signaling Complex. *Sci. Adv.* **2021**, *21* (7), eabg5628.

(37) Zhou, F.; Ye, C.; Ma, X.; Yin, W.; Croll, T. I.; Zhou, Q.; He, X.; Zhang, X.; Yang, D.; Wang, P.; Xu, H. E.; Wang, M. W.; Jiang, Y. Molecular Basis of Ligand Recognition and Activation of Human V2 Vasopressin Receptor. *Cell Res.* **2021**, *31* (8), 929–931. https://doi.org/10.1038/s41422-021-00480-2.

(38) Wang, L.; Xu, J.; Cao, S.; Sun, D.; Liu, H.; Lu, Q.; Liu, Z.; Du, Y.; Zhang, C. Cryo-EM Structure of the AVP–Vasopressin Receptor 2–Gs Signaling Complex. *Cell Res.* **2021**, *31* (8), 932–934. https://doi.org/10.1038/S41422-021-00483-Z.

(39) Bous, J.; Fouillen, A.; Orcel, H.; Trapani, S.; Cong, X.; Fontanel, S.; Saint-Paul, J.; Lai-Kee-Him, J.; Urbach, S.; Sibille, N.; Sounier, R.; Granier, S.; Mouillac, B.; Bron, P. Structure of the Vasopressin Hormone-V2 Receptor-β-Arrestin1 Ternary Complex. *Sci. Adv.* **2022**, *10.1126/sc*, in press. https://doi.org/10.1101/2022.02.11.480047.

(40) Bokoch, M. P.; Zou, Y.; Rasmussen, S. G. F.; Liu, C. W.; Nygaard, R.; Rosenbaum, D. M.; Fung, J. J.; Choi, H. J.; Thian, F. S.; Kobilka, T. S.; Puglisi, J. D.; Weis, W. I.; Pardo, L.; Prosser, R. S.; Mueller, L.; Kobilka, B. K. Ligand-Specific Regulation of the Extracellular Surface of a G-Protein-Coupled Receptor. *Nature* **2010**, *463* (7277), 108–112. https://doi.org/10.1038/nature08650.

(41) Sounier, R.; Mas, C.; Steyaert, J.; Laeremans, T.; Manglik, A.; Huang, W.; Kobilka, B. K.; Déméné, H.; Granier, S. Propagation of Conformational Changes during μ-Opioid Receptor Activation. *Nature* **2015**, *524* (7565), 375–378. https://doi.org/10.1038/nature14680.

(42) Kimbrough, R. D. J.; Cash, W. D.; Branda, L. A.; Chan, W.; Du Vigneau, V. Synthesis and Biological Properties of 1-Desamino-8-Lysine-Vasopressin. *J. Biol. Chem.* **1963**, *238* (4), 1411–1414. https://doi.org/10.1016/S0021-9258(18)81197-8.

(43) Zhou, F.; Ye, C.; Ma, X.; Yin, W.; Croll, T. I.; Zhou, Q.; He, X.; Zhang, X.; Yang, D.; Wang, P.; Xu, H. E.; Wang, M. W.; Jiang, Y. Molecular Basis of Ligand Recognition and Activation of Human V2 Vasopressin Receptor. *Cell Res.* **2021**, *31* (8), 929–931. https://doi.org/10.1038/S41422-021-00480-2.

(44) Huang, S. K.; Pandey, A.; Tran, D. P.; Villanueva, N. L.; Kitao, A.; Sunahara, R. K.; Sljoka, A.; Prosser, R. S. Delineating the Conformational Landscape of the Adenosine A2A Receptor during G Protein Coupling. *Cell* **2021**, *184* (7), 1884-1894.e14. https://doi.org/10.1016/j.cell.2021.02.041.

(45) Mirzadegan, T.; Benko, G.; Filipek, S.; Palczewski, K. Sequence Analyses of G-Protein-Coupled Receptors: Similarities to Rhodopsin. *Biochemistry* **2003**, *42* (10), 2759. https://doi.org/10.1021/bi027224+.

(46) Kosugi, S.; Hai, N.; Okamoto, H.; Sugawa, H.; Mori, T. A Novel Activating Mutation in the Thyrotropin Receptor Gene in an Autonomously Functioning Thyroid Nodule Developed by a Japanese Patient. *Eur. J. Endocrinol.* **2000**, *143* (4), 471–477. https://doi.org/10.1530/EJE.0.1430471.

(47) Trülzsch, B.; Krohn, K.; Wonerow, P.; Chey, S.; Holzapfel, H. P.; Ackermann, F.; Führer, D.; Paschke, R. Detection of Thyroid-Stimulating Hormone Receptor and Gsalpha Mutations: In 75 Toxic Thyroid Nodules by Denaturing Gradient Gel Electrophoresis. *J. Mol. Med. (Berl).* **2001**, *78* (12), 684–691. https://doi.org/10.1007/S001090000170.

(48) Tao, Y. X.; Abell, A. N.; Liu, X.; Nakamura, K.; Segaloff, D. L. Constitutive Activation of G Protein-Coupled Receptors as a Result of Selective Substitution of a Conserved Leucine Residue in Transmembrane Helix III. *Mol. Endocrinol.* **2000**, *14* (8), 1272–1282. https://doi.org/10.1210/mend.14.8.0503.

(49) Lu, Z. L.; Hulme, E. C. The Functional Topography of Transmembrane Domain 3 of the M1 Muscarinic Acetylcholine Receptor, Revealed by Scanning Mutagenesis. *J. Biol. Chem.* **1999**, *274* (11), 7309–7315. https://doi.org/10.1074/JBC.274.11.7309.

(50) Baranski, T. J.; Herzmark, P.; Lichtarge, O.; Gerber, B. O.; Trueheart, J.; Meng, E. C.; Iiri, T.; Sheikh, S. P.; Bournet, H. R. C5a Receptor Activation. Genetic Identification of Critical Residues in Four Transmembrane Helices. *J. Biol. Chem.* **1999**, *274* (22), 15757–15765. https://doi.org/10.1074/JBC.274.22.15757.

(51) Ceraudo, E.; Horioka, M.; Mattheisen, J. M.; Hitchman, T. D.; Moore, A. R.; Kazmi, M. A.; Chi, P.; Chen, Y.; Sakmar, T. P.; Huber, T. Direct Evidence That the GPCR CysLTR2 Mutant Causative of Uveal Melanoma Is Constitutively Active with Highly Biased Signaling. *J. Biol. Chem.* **2021**, *296*, 100163. https://doi.org/10.1074/jbc.RA120.015352.

(52) Mo, X. L.; Yang, R.; Tao, Y. X. Functions of Transmembrane Domain 3 of Human Melanocortin-4 Receptor. *J. Mol. Endocrinol.* **2012**, *49* (3), 221–235. https://doi.org/10.1530/JME-12-0162.

(53) McCorvy, J. D.; Wacker, D.; Wang, S.; Agegnehu, B.; Liu, J.; Lansu, K.; Tribo, A. R.; Olsen, R. H. J.; Che, T.; Jin, J.; Roth, B. L. Structural Determinants of 5-HT2B Receptor Activation and Biased Agonism. *Nat Struct Mol Biol* **2018**, *25* (9), 787–796.

(54) Cao, D.; Yu, J.; Wang, H.; Luo, Z.; Liu, X.; He, L.; Qi, J.; Fan, L.; Tang, L.; Chen, Z.; Li, J.; Cheng, J.; Wang, S. Structure-Based Discovery of Nonhallucinogenic Psychedelic Analogs. *Science* **2022**, *375* (6579), 403–411. https://doi.org/10.1126/SCIENCE.ABL8615.

(55) Shao, Z.; Shen, Q.; Yao, B.; Mao, C.; Chen, L. N.; Zhang, H.; Shen, D. D.; Zhang, C.; Li, W.; Du, X.; Li, F.; Ma, H.; Chen, Z. H.; Xu, H. E.; Ying, S.; Zhang, Y.; Shen, H. Identification and Mechanism of G Protein-Biased Ligands for Chemokine Receptor CCR1. *Nat. Chem. Biol.* **2021**, *18* (March). https://doi.org/10.1038/s41589-021-00918-z.

(56) Wacker, D.; Wang, C.; Katritch, V.; Han, G. W.; Huang, X. P.; Vardy, E.; McCorvy, J. D.; Jiang, Y.; Chu, M.; Siu, F. Y.; Liu, W.; Xu, H. E.; Cherezov, V.; Roth, B. L.; Stevens, R. C. Structural Features for Functional Selectivity at Serotonin Receptors. *Science (80-.).* **2013**, *340* (6132), 615–619. https://doi.org/10.1126/science.1232808.

(57) McCorvy, J. D.; Butler, K. V.; Kelly, B.; Rechsteiner, K.; Karpiak, J.; Betz, R. M.; Kormos, B. L.; Shoichet, B. K.; Dror, R.

O.; Jin, J.; Roth, B. L. Structure-Inspired Design of β-Arrestin-Biased Ligands for Aminergic GPCRs. *Nat. Chem. Biol.* **2018**, *14* (2), 126–134. https://doi.org/10.1038/NCHEMBIO.2527.

(58) Xu, P.; Huang, S.; Zhang, H.; Mao, C.; Zhou, X. E.; Cheng, X.; Simon, I. A.; Shen, D. D.; Yen, H. Y.; Robinson, C. V.; Harpsøe, K.; Svensson, B.; Guo, J.; Jiang, H.; Gloriam, D. E.; Melcher, K.; Jiang, Y.; Zhang, Y.; Xu, H. E. Structural Insights into the Lipid and Ligand Regulation of Serotonin Receptors. *Nature* **2021**, *592* (7854), 469–473. https://doi.org/10.1038/s41586-021-03376-8.

(59) Peng, Y.; McCorvy, J. D.; Harpsøe, K.; Lansu, K.; Yuan, S.; Popov, P.; Qu, L.; Pu, M.; Che, T.; Nikolajsen, L. F.; Huang, X. P.; Wu, Y.; Shen, L.; Bjørn-Yoshimoto, W. E.; Ding, K.; Wacker, D.; Han, G. W.; Cheng, J.; Katritch, V.; Jensen, A. A.; Hanson, M. A.; Zhao, S.; Gloriam, D. E.; Roth, B. L.; Stevens, R. C.; Liu, Z. J. 5-HT2C Receptor Structures Reveal the Structural Basis of GPCR Polypharmacology. *Cell* **2018**, *172* (4), 719-730.e14. https://doi.org/10.1016/j.cell.2018.01.001.

(60) Schönegge, A. M.; Gallion, J.; Picard, L. P.; Wilkins, A. D.; Le Gouill, C.; Audet, M.; Stallaert, W.; Lohse, M. J.; Kimmel, M.; Lichtarge, O.; Bouvier, M. Evolutionary Action and Structural Basis of the Allosteric Switch Controlling β 2 AR Functional Selectivity. *Nat. Commun.* **2017**, *8* (1). https://doi.org/10.1038/S41467-017-02257-X.

(61) Wingler, L. M.; McMahon, C.; Staus, D. P.; Lefkowitz, R. J.; Kruse, A. C. Distinctive Activation Mechanism for Angiotensin Receptor Revealed by a Synthetic Nanobody. *Cell* **2019**, 1–12. https://doi.org/10.1016/j.cell.2018.12.006.

(62) Asher, W. B.; Terry, D. S.; Gregorio, G. G. A.; Kahsai, A. W.; Borgia, A.; Xie, B.; Modak, A.; Zhu, Y.; Jang, W.; Govindaraju, A.; Huang, L.-Y.; Inoue, A.; Lambert, N. A.; Gurevich, V. V; Shi, L.; Lefkowitz, R. J.; Blanchard, S. C.; Javitch, J. A. GPCR-Mediated β-Arrestin Activation Deconvoluted with Single-Molecule Precision. *Cell* **2022**, *185* (10). https://doi.org/10.1016/J.CELL.2022.03.042.

(63) Gmeiner, P.; Wang, H.; Hetzer, F.; Huang, W.; Qu, Q.; Meyerowitz, J.; Kaindl, J.; Hübner, H.; Skiniotis, G.; Kobilka, B. K. Structure-Based Evolution of G Protein-Biased μ-Opioid Receptor Agonists. *Angew. Chem. Int. Ed. Engl.* **2022**. https://doi.org/10.1002/ANIE.202200269.

(64) Morello, J. P.; Bouvier, M.; Petäjä-Repo, U. E.; Bichet, D. G. Pharmacological Chaperones: A New Twist on Receptor Folding. *Trends Pharmacol. Sci.* **2000**, *21* (12), 466–469. https://doi.org/10.1016/S0165-6147(00)01575-3.

(65) Delaglio, F.; Grzesiek, S.; Vuister, G. W.; Zhu, G.; Pfeifer, J.; Bax, A. NMRPipe: A Multidimensional Spectral Processing System Based on UNIX Pipes. *J. Biomol. NMR 1995 63* **1995**, *6* (3), 277–293. https://doi.org/10.1007/BF00197809.

(66) Johnson, B. A.; Blevins, R. A. NMR View: A Computer Program for the Visualization and Analysis of NMR Data. *J. Biomol. NMR 1994 45* **1994**, *4* (5), 603–614. https://doi.org/10.1007/BF00404272.

(67) Loison, S.; Cottet, M.; Orcel, H.; Adihou, H.; Rahmeh, R.; Lamarque, L.; Trinquet, E.; Kellenberger, E.; Hibert, M.; Durroux, T.; Mouillac, B.; Bonnet, D. Selective Fluorescent Nonpeptidic Antagonists For Vasopressin V 2 GPCR: Application To Ligand Screening and Oligomerization Assays. *J. Med. Chem.* **2012**, *55* (20), 8588–8602. https://doi.org/10.1021/jm3006146.

(68) Zwier, J. M.; Roux, T.; Cottet, M.; Durroux, T.; Douzon, S.; Bdioui, S.; Gregor, N.; Bourrier, E.; Oueslati, N.; Nicolas, L.; Tinel, N.; Boisseau, C.; Yverneau, P.; Charrier-Savournin, F.; Fink, M.; Trinquet, E. A Fluorescent Ligand-Binding Alternative Using Tag-Lite® Technology. *J. Biomol. Screen.* **2010**, *15* (10), 1248–1259. https://doi.org/10.1177/1087057110384611.

(69) Tenenbaum, J.; Ayoub, M. A.; Perkovska, S.; Adra-Delenne, A. L.; Mendre, C.; Ranchin, B.; Bricca, G.; Geelen, G.; Mouillac, B.; Durroux, T.; Morin, D. The Constitutively Active V2 Receptor Mutants Conferring NSIAD Are Weakly Sensitive to Agonist and Antagonist Regulation. *PLoS One* **2009**, *4* (12), e8383.

(70) Waltenspühl, Y.; Schöppe, J.; Ehrenmann, J.; Kummer, L.; Plückthun, A. Crystal Structure of the Human Oxytocin Receptor. *Sci. Adv.* **2020**, *6* (29), 1–12. https://doi.org/10.1126/sciadv.abb5419.

(71) Schott-Verdugo, S.; Gohlke, H. PACKMOL-Memgen: A Simple-To-Use, Generalized Workflow for Membrane-Protein-Lipid-Bilayer System Building. *J. Chem. Inf. Model.* **2019**, *59* (6). https://doi.org/10.1021/ACS.JCIM.9B00269.

(72) Lindorff-Larsen, K.; Piana, S.; Palmo, K.; Maragakis, P.; Klepeis, J. L.; Dror, R. O.; Shaw, D. E. Improved Side-Chain Torsion Potentials for the Amber Ff99SB Protein Force Field. *Proteins* **2010**, *78* (8), 1950–1958. https://doi.org/10.1002/PROT.22711.

(73) Wang, J.; Wolf, R. M.; Caldwell, J. W.; Kollman, P. A.; Case, D. A. Development and Testing of a General Amber Force Field. *J. Comput. Chem.* **2004**, *25* (9), 1157–1174. https://doi.org/10.1002/JCC.20035.

(74) Dickson, C. J.; Madej, B. D.; Skjevik, Å. A.; Betz, R. M.; Teigen, K.; Gould, I. R.; Walker, R. C. Lipid14: The Amber Lipid Force Field. *J. Chem. Theory Comput.* **2014**, *10* (2), 865–879. https://doi.org/10.1021/CT4010307.

(75) Jorgensen, W. L.; Chandrasekhar, J.; Madura, J. D.; Impey, R. W.; Klein, M. L. Comparison of Simple Potential Functions for Simulating Liquid Water. *J. Chem. Phys.* **1998**, *79* (2), 926. https://doi.org/10.1063/1.445869.

(76) Joung, I. S.; Cheatham, T. E. Determination of Alkali and Halide Monovalent Ion Parameters for Use in Explicitly Solvated Biomolecular Simulations. *J. Phys. Chem. B* **2008**, *112* (30), 9020–9041. https://doi.org/10.1021/JP8001614/SUPPL_FILE/JP8001614-FILE003.PDF.

(77) Wang, J.; Cieplak, P.; Kollman, P. How Well Does a Restrained Electrostatic Potential (RESP) Model Perform in Calculating Conformational Energies of Organic and Biological Molecules? - Wang - 2000 - Journal of Computational Chemistry - Wiley Online Library. *J. Compuational Chem.* **2000**, *21*, 12.

(78) Van Der Spoel, D.; Lindahl, E.; Hess, B.; Groenhof, G.; Mark, A. E.; Berendsen, H. J. C. GROMACS: Fast, Flexible, and Free. *J. Comput. Chem.* **2005**, *26* (16), 1701–1718. https://doi.org/10.1002/JCC.20291.

(79) Tribello, G.; Bonomi, M.; Branduardi, D.; Bussi, C. PLUMED 2: New Feathers for an Old Bird - Research - Institut Pasteur. *Comput. Phys. Commun.* **2014**, *185*, 604–613.

(80) Wang, L.; Friesner, R. A.; Berne, B. J. Replica Exchange with Solute Scaling: A More Efficient Version of Replica Exchange with Solute Tempering (REST2). *J. Phys. Chem. B* **2011**, *115* (30), 9431–9438. https://doi.org/10.1021/jp204407d.

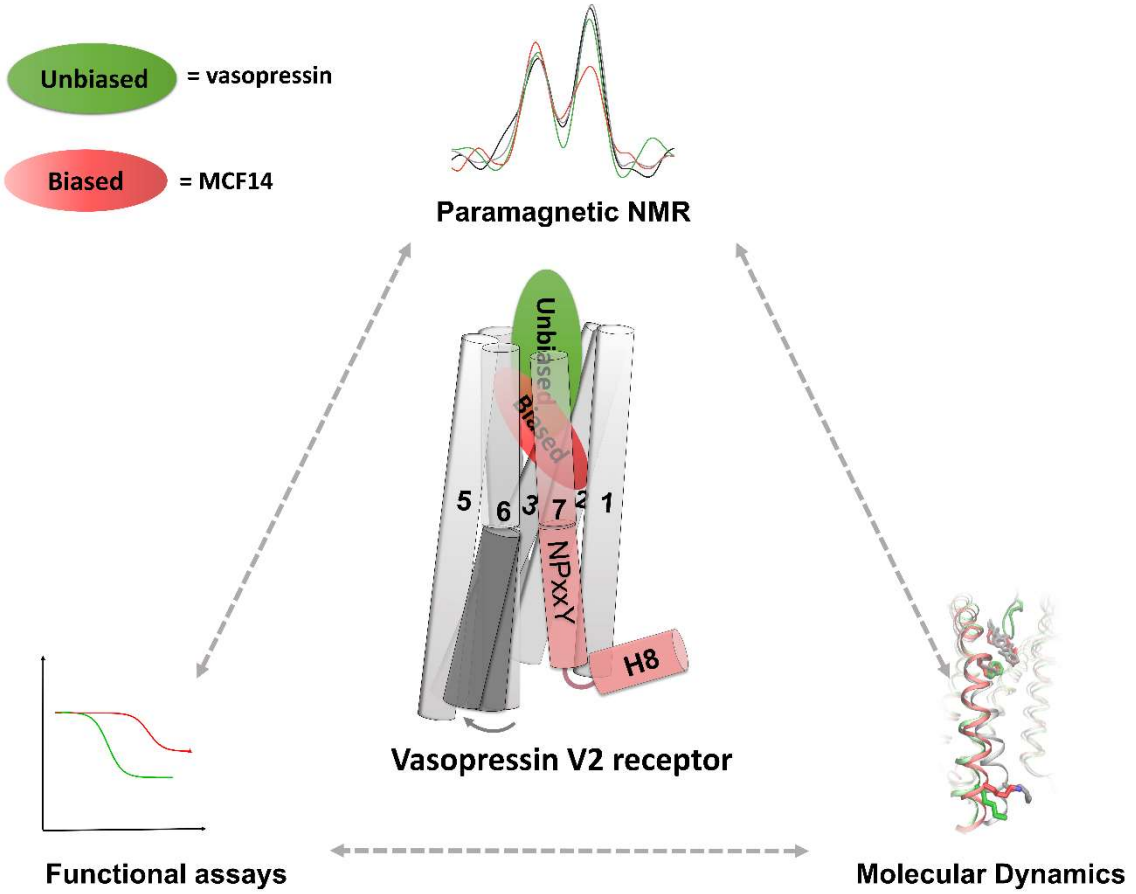
Unbiased
= vasopressin
Biased
= MCF14
Paramagnetic NMR
Unbiased
Biased
5
6
3
7
2
1
NPXXY
H8
Vasopressin V2 receptor
Functional assays
Molecular Dynamics

Biased activation of the vasopressin V2 receptor probed by NMR, paramagnetic ligands and molecular simulations.

Gérald Gaibelet,[†,$,#] Aurélien Fouillen,[†,⁋,#] Stéphanie Riché,[‡] Hélène Orcel,[†] Christiane Mendre,[†] Romain Lanotte,[†] Julie N'Guyen,[†] Rémy Sounier,[†] Sébastien Granier,[†] Dominique Bonnet,[‡] Xiaojing Cong,[†,*] Bernard Mouillac,[†,*] Hélène Déméné[⁋,*]

[†]Institut de Génomique Fonctionnelle, Université de Montpellier, CNRS, INSERM, 34094 Montpellier cedex 5, France.

[⁋]Centre de Biologie Structurale, Univ Montpellier, INSERM, CNRS, 34090 Montpellier, France

[‡] Laboratoire d'Innovation Thérapeutique, UMR7200 CNRS, Université de Strasbourg, Institut du Médicament de Strasbourg, 67412 Illkirch-Graffenstaden, France.

[$] Present address, AB Science, 13288 Marseille cedex 9, France

[#] These authors contributed equally to the work.

Table of Contents

Table S1. Ligand binding affinity for wild type (wt) V2R and variants.

Receptor	K_d Benzazepine-red (nM)	K_i AVP (nM)
wt V2R	2.3 ± 0.3[a]	0.9 ± 0.3 (n=5)
V2R-K100R	2.30 ± 1	3.2 ± 2.1
V2R-K116R	8.5 ± 1.9	3.4 ± 0.8
V2R-K268R	2.9 ± 1.3	2.0 ± 1.3
V2R-I130N	6.6 ± 2.5	1.4 ± 0.6

[a] from ref. (1).

Competitive binding experiments were performed as detailed in Materials and Methods, using the benzazepine-red fluorescent ligand as a tracer. Specific binding of the benzazepine-red antagonist is calculated as a FRET ratio (665nm/620nm). K_d and K_i values are mean ± SEM (n = 3, unless otherwise indicated).

Table S2. Ligand binding affinity and potency for V2R-K100R variant.

		cAMP accumulation
	Ki (nM)	EC50 (nM)
AVP	3.2 ± 2.1	0.12 ± 0.05
MCF14	11.4 ± 0.4	26.9 ± 3.3
Tolvaptan	1.3 ± 0.4	n.a[a]

[a] n.a: not applicable

Competitive binding experiments were performed as detailed in Materials and Methods, using the benzazepine-red fluorescent ligand as a tracer. Specific binding of the benzazepine-red antagonist is calculated as a FRET ratio (665nm/620nm). Accumulation of cAMP is calculated as a FRET ratio (665nm/620nm) and measured in the presence of increasing concentrations of ligands (AVP, MCF14, TVP). K_i and EC50 values are mean ± SEM (n = 3).

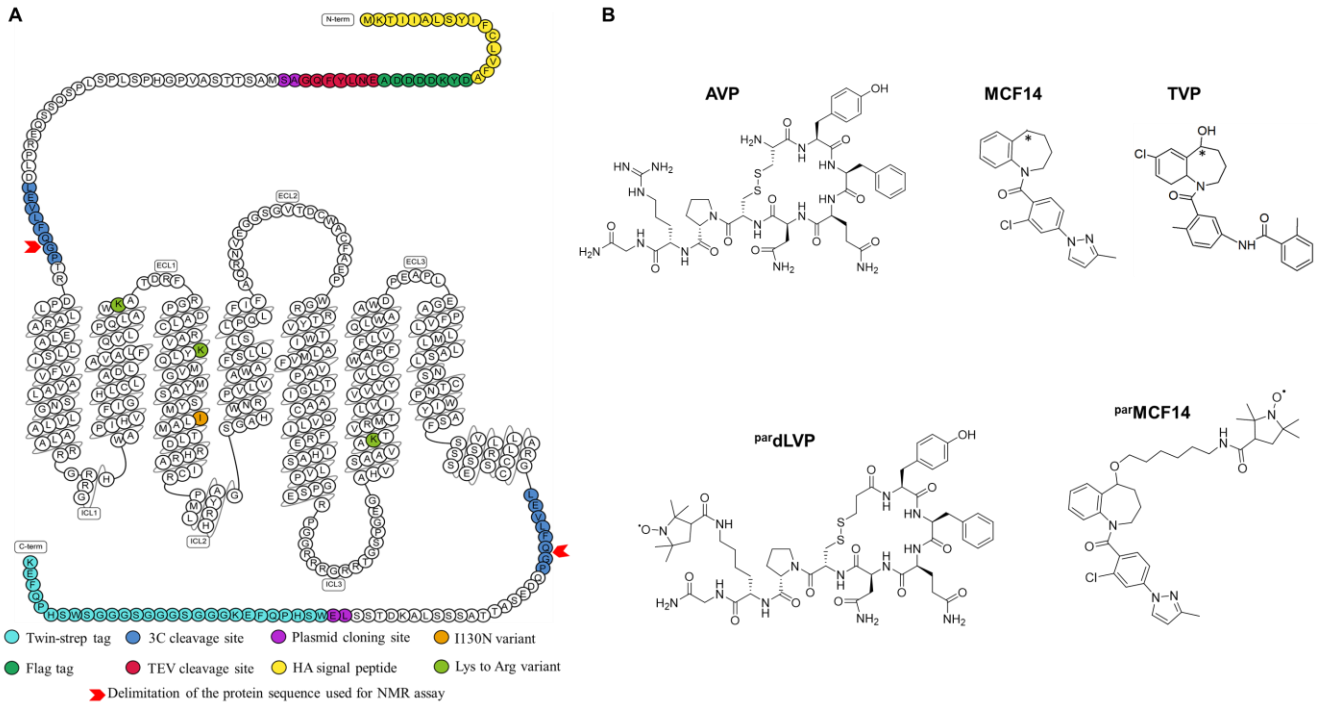

Figure S1. Engineering of ligands and V2R. (A) Snake plot of the V2R sequence used in this study. The hemagglutinin (HA) signal peptide (MKTIIALSYIFCLVFA, in yellow) followed by a Flag tag (DYKDDDDA, in dark green) and a TEV protease cleavage site (ENLYFQG, in red) were added at the N-terminus, while a Twin-strep-tag® (WSHPQFEKGGGSGGGSGGGSWSHPQFEK, in cyan) was inserted at the C-terminus. In addition, N22 was substituted with a glutamine residue to avoid N-glycosylation, and C358 mutated into an alanine to eliminate potential intermolecular disulfide bridges during solubilization and purification. Two HRV3C protease cleavage sites (LEVLFQGP, in blue) were also added to remove the N- and C-termini and enhance the NMR spectra quality, one in the N-terminus between D30 and T31 and one in the C-terminus between G345 and Q354 (replacing R346-TPPSLG-P353), indicated by two red arrows. M1 and L2 residues after truncation were replaced by A and S residues (purple), and LE residues (purple) were added just before the Twin-strep-tag®, during subcloning (by introduction of a Nhe1 and a Xho1 restriction site, respectively). Mutation sites of K100$^{2.65}$R, K116$^{3.29}$R, K268$^{6.32}$R and I130$^{3.43}$N are indicated in light green and orange. Arrows indicate N- and C-termini of the V2R protein after HRV3C cleavage **(B)** Chemical structures of the ligands (see Figure S3 for the synthesis). The chiral center of TVP and ^{par}MCF14 is labeled by an asterisk.

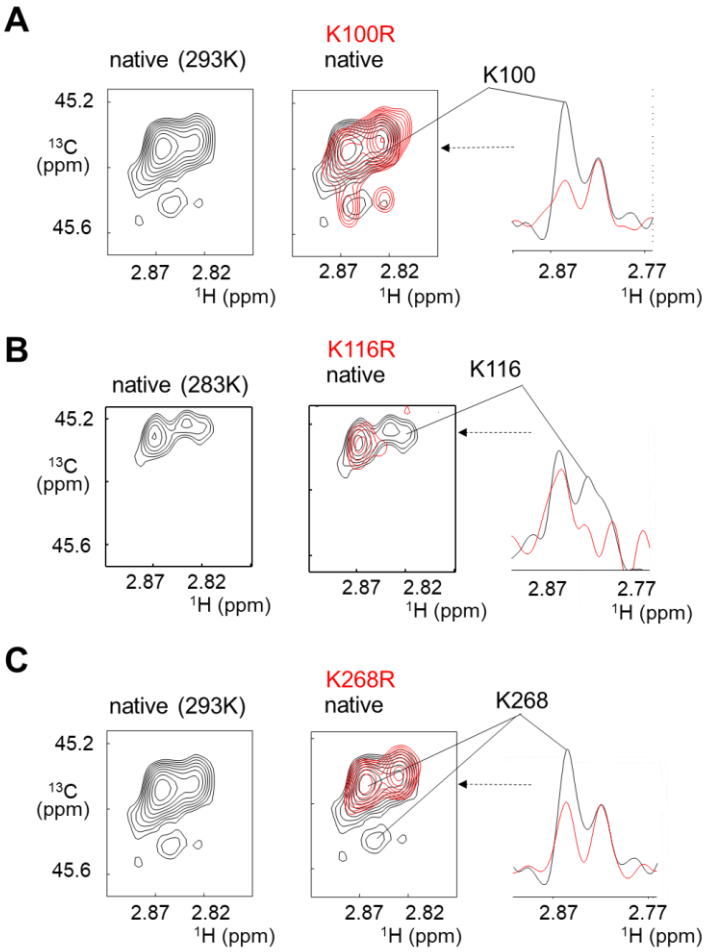

Figure S2. Assignment of correlation peaks of dimethylated lysines. Extracted HMQC spectrum of native V2R (black) is superimposed on that of the mutants (red): **(A)** K100$^{2.65}$R, **(B)** K268$^{6.32}$R and **(C)** K116$^{3.29}$R. Experiments were run at 293 K, except for the assignment of the K116 resonance (B). On the right panels, we

highlight the peak disappearance for each mutant (red line) as compared to native V2R (black line) in the ^{1}H dimension.

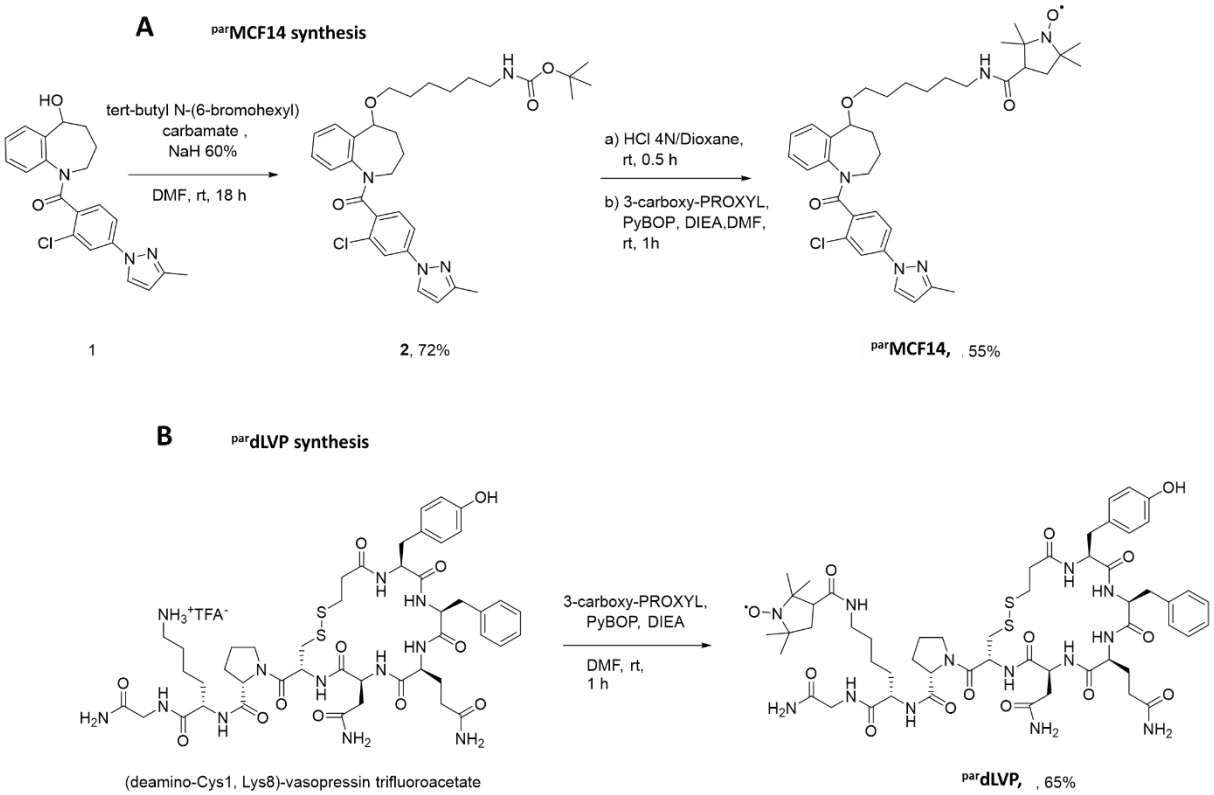

Figure S3. Synthesis of paramagnetic ligands. (A) ^{par}MCF14 and **(B)** ^{par}dLVP. The procedures are fully detailed in the supplementary methods section.

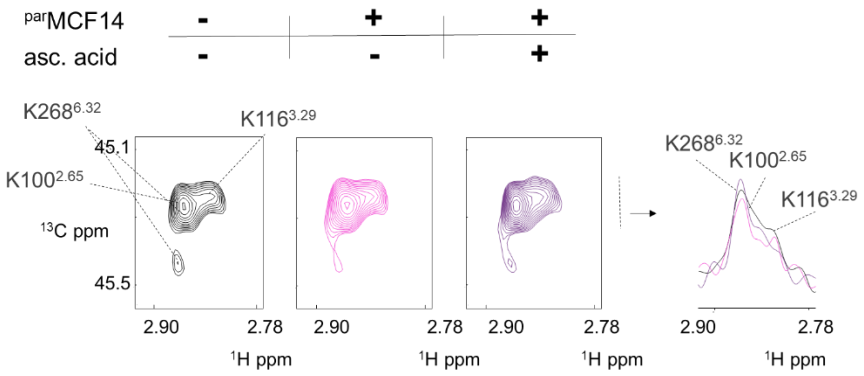

Figure S4. Effect of ^{par}MCF14 binding and reduction by ascorbic acid on the lysine HMQC correlation peaks of wt V2R. The 1D projection along the ^{13}C dimension of ^{1}H rows is indicated by an arrow, showing a specific effect according to each lysine.

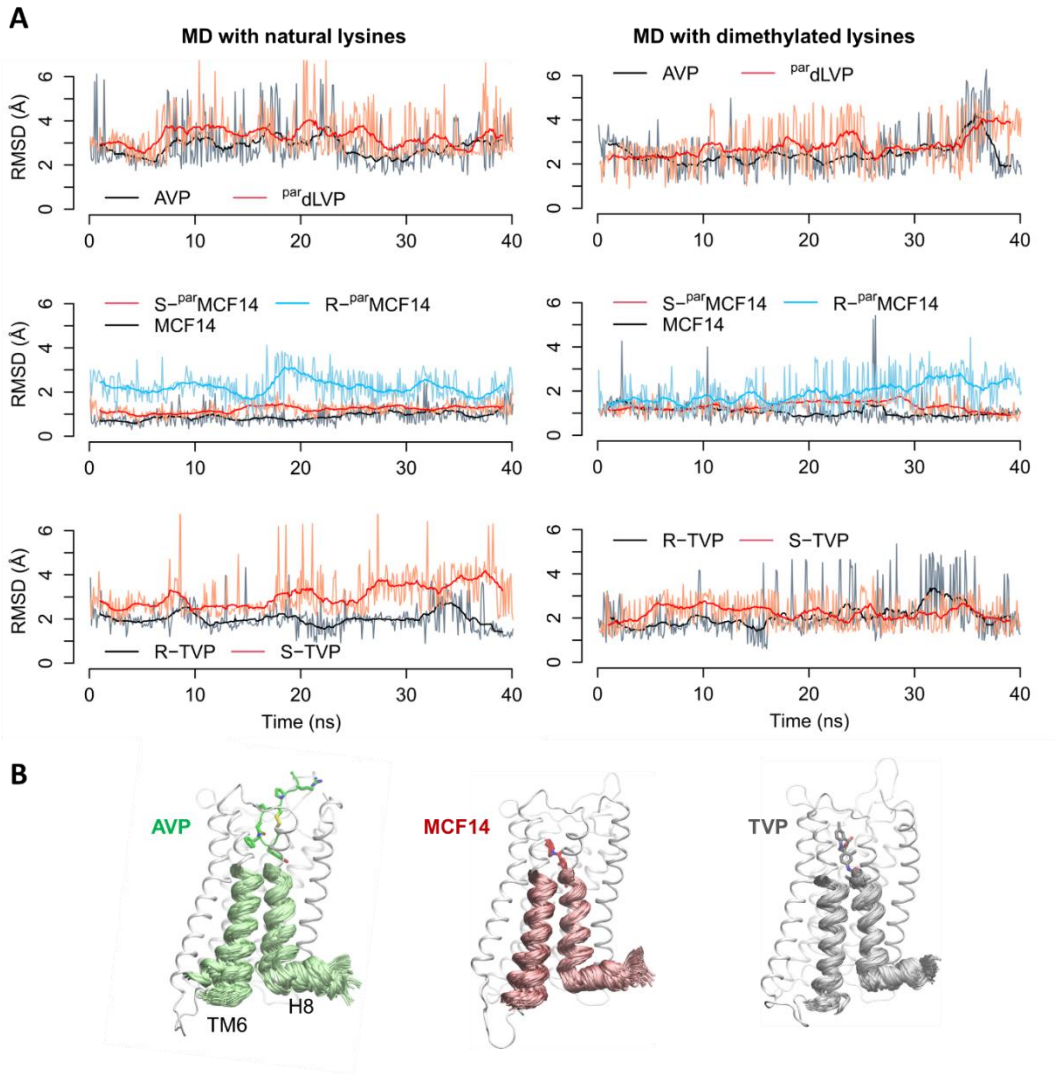

Figure S5. Conformational dynamics of V2R and ligands during MD simulations. (A) Ligand RMSD calculated for the heavy atoms of MCF14 and TVP, or the backbone atoms of AVP and ^{par}dLVP, excluding the paramagnetic tag. The same trends are observed in the simulations with dimethylated and natural lysines. **(B)** Movements of TM6, TM7 and H8 on the intracellular side of V2R in the simulations with natural lysines.

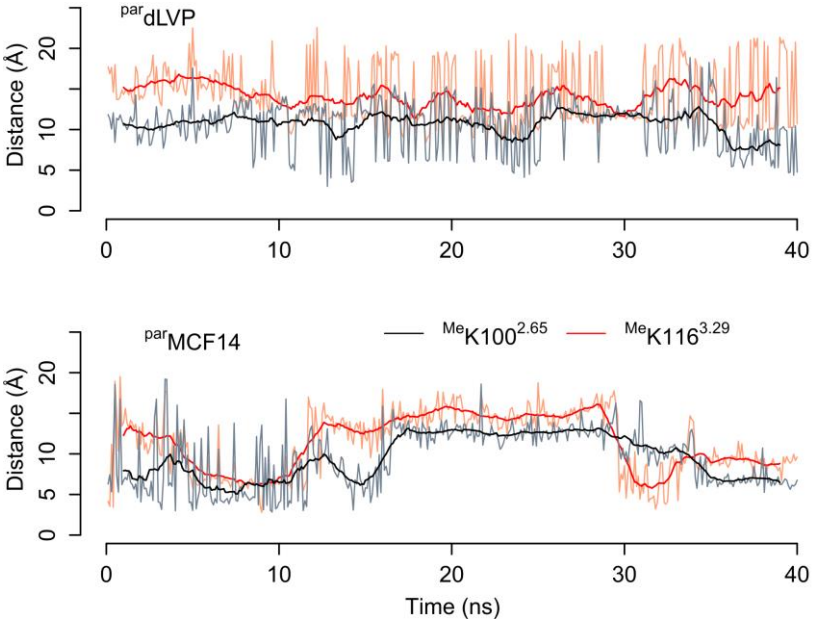

Figure S6. Distances between the paramagnetic tag and dimethylated K100$^{2.65}$ and K116$^{3.29}$ during the MD simulations. The distance is measured between the nitroxide oxygen atom and nitrogen atom of the lysine side chain.

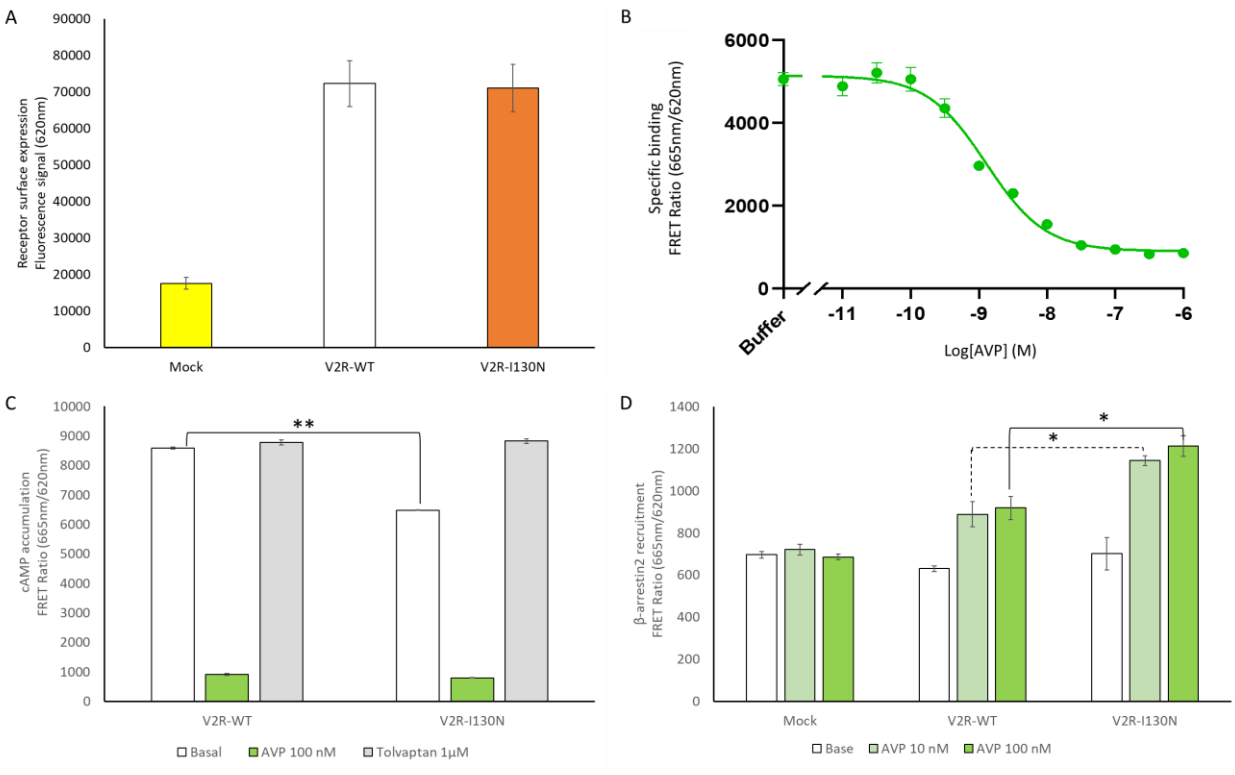

(A)

Figure S7. Pharmacological and functional properties of the mutant V2R-I130N. (A) Evaluation of the receptor expression level at the cell surface by measuring the fluorescence signal at 620 nm (see Materials and Methods for details). The expression of the I130N mutant is compared to that of wt V2R. (**B**) Binding of AVP to the mutant V2R-I130N is illustrated as the FRET ratio (665nm/620nm x 10,000). Specific binding of the fluorescent benzazepine-red antagonist is shown. For each competition curve, the tracer was used at 5 nM with or without increasing concentrations of AVP. (**C**) Basal and ligand-induced V2R-dependent cAMP accumulation measured by the FRET ratio (665nm/620nm x 10,000). The functional properties of the mutant V2R-I130N are compared to those of wt V2R. The cAMP accumulation is compared to that measured in the presence of 100 nM of AVP (in green) or 1 µM of TVP (in grey). (**D**) V2R-dependent recruitment of βarr2 to AP2 measured by the FRET ratio (665nm/620nm x 10,000) in the presence of 0 nM (basal), 10 nM or 100 nM of AVP. The capacity of β-arrestin2 recruitment of the mutant V2R-I130N is compared to that of wt V2R. Data are mean ± SEM of 3 technical replicates where statistical significance is assessed by T-test (*, $p < 0.05$; **, $p < 0.01$).

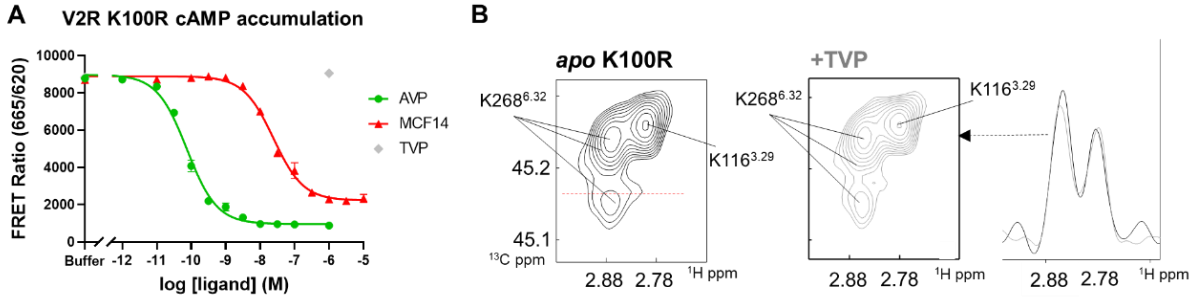

Figure S8. Functional properties of the V2R-K100R mutant. (A) Ligand dose-response curves of V2R-dependent cAMP accumulation measured by FRET ratio (665nm/620nm x 10,000). The cAMP accumulation was quantified using the cAMP Dynamic 2 kit (PerkinElmer CisBio) as indicated in Materials and Methods and is shown in the presence of increasing concentrations of AVP (green), MCF14 (red), and TVP (in grey). Data are mean ± SEM of 3 technical replicates. **(B)** Extracted HMQC spectra of the K100R mutant in *apo* form (black) and in the presence of saturating concentrations of the TVP antagonist (grey). The spectra of the *apo* and TPV-bound states are almost identical, indicating that the *apo* form is mainly inactive.

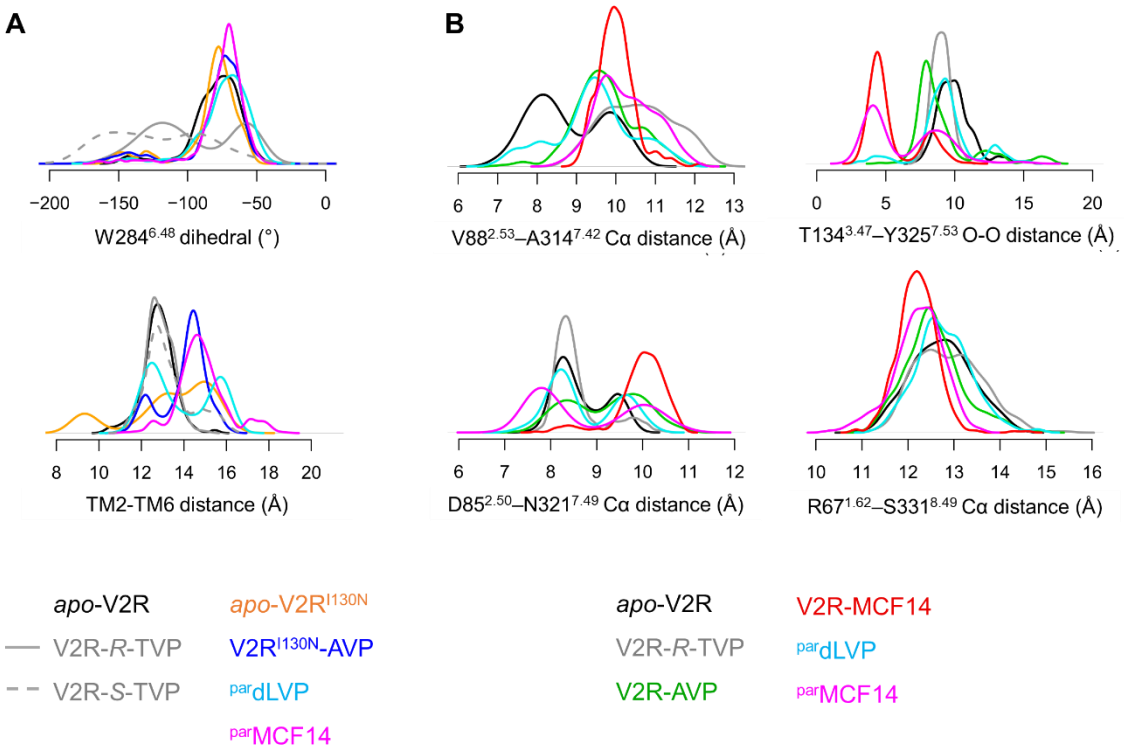

Figure S9: Probability density distribution of the conformational features measured during the MD simulations. (A) and **(B)** are supplementary to Figure 3 and Figures **4** and **5**, respectively.

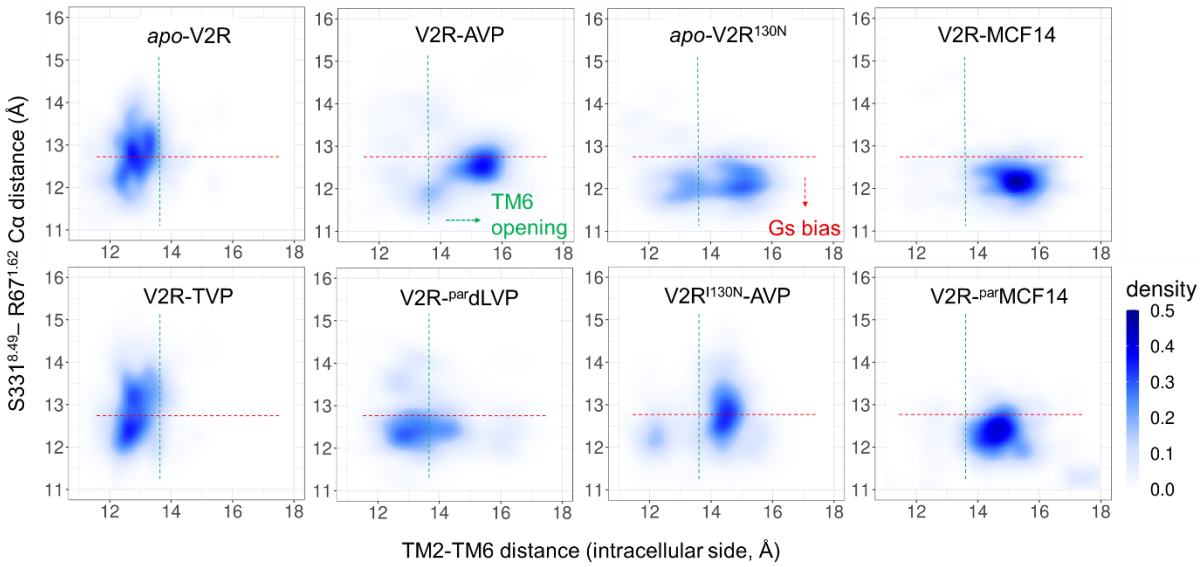

Figure S10. Probability density map of two conformational features during the MD simulations. TM6 opening (*x*-axis) is considered as an indicator of the canonical activation, whereas H8-TM1 closure (*y*-axis) is used as an indicator of the G-protein bias. TM6 opening is measured by the center-of-mass distance between the backbones of I74$^{2.39}$-F77$^{2.42}$ and V266$^{6.30}$-T269$^{6.33}$. H8-TM1 closure is measured by the Cα distance between S331$^{8.49}$ and R67$^{1.62}$.

Supplementary Methods for REST2 MD simulations.

REST2[2] is a type of Hamiltonian replica exchange simulation scheme, which performs many replicas of the same MD simulation system in parallel with the original system. The replicas have modified free energy surfaces to facilitate barrier crossing. By frequently swapping the replicas and the original system during the MD, the simulations "travel" on different free energy surfaces and easily visit different conformational zones. Finally, only the samples in the original system (with unmodified free energy surface) are collected. The replicas are artificial and are only used to overcome the energy barriers. REST2 modifies the free energy surfaces by scaling (reducing) the force constants of the "solute" molecules in the simulation system. In this case, the protein and the ligands were considered as "solute"–the force constants of their van der Waals, electrostatic and dihedral terms were subject to scaling–in order to facilitate their conformational changes. The effective temperatures used here for generating the REST2 scaling factors ranged from 310 K to 1000 K for 64 replicas, following a distribution calculated with the Patriksson-van der Spoel approach.[3] Exchange between the replicas was attempted every 1000 simulation steps. This setup resulted in an average exchange probability of ~30 % throughout the simulation course.

Supplementary methods for pharmacology

Statistical analysis. For pharmacology assays, values and SEM were calculated from at least three independent experiments, and the p values were obtained by T-test analysis of each condition from data in Excel (Microsoft Windows, Albuquerque, NM, USA). Statistical significance was defined as ns, $p > 0.05$; *$p < 0.05$; **$p < 0.01$; ***$p < 0.001$; and ****$p < 0.0001$.

Supplementary methods for chemistry

General

Reagents were obtained from commercial sources and used without any further purification. (Deamino-Cys[1], Lys[8])-Vasopressin trifluoroacetate was purchased from Bachem. Compound **1** was synthesized as previously described.[4] Thin-layer chromatography was performed on Merck silica gel 60F254 plates. VWR silica gel (40-63 µm) was used for chromatography columns. Semi-preparative reverse-phase HPLC purifications were performed on a Waters SunFire C18 OBD Prep column (5 µm, 19 × 150 mm) on a Gilson PLC2020 system. Analytical reverse-phase HPLC were performed on a Ascentis C18 column (2.7 µm, 7.5 cm × 4.6 mm) on an Agilent Technologies 1200 series HPLC system using a linear gradient (5% to 100% v/v in 7.3 min, flow rate of 1.6 mL.min-1) of solvent B (0.1% v/v TFA in CH_3CN) in solvent A (0.1% v/v TFA in H_2O). ^{1}H NMR spectra were recorded at 400 MHz, ^{13}C NMR spectra were recorded at 101 MHz on a Bruker Advance spectrometer. Chemical shifts are reported in parts per million (ppm), and coupling constants (J) are reported in hertz (Hz). Signals are described as s (singlet), d (doublet), t (triplet), q (quadruplet), p (pentuplet) and m (multiplet). High-resolution mass spectra (HRMS) were obtained on an Agilent Technologie 6520 Accurare-Mass Q.Tof LC/MS apparatus equipped with a Zorbax SB C18 column (1.8 µm, 2.1 × 50 mm) using electrospray ionization (ESI) and a time-of-flight analyzer (TOF).

Synthesis of paramagnetic ligands

^{par}MCF14

The synthesis of ^{par}MCF14 was performed in two steps (see Figure S3).

Tert-butyl (6-((1-(2-chloro-4-(3-methyl-1H-pyrazol-1-yl) benzoyl)-2,3,4,5-tetrahydro-1H-benzo[b]azepin-5-yl) oxy)hexyl)carbamate (2). To a solution of **1** (281.6 mg, 0.74 mmol) in 20 mL of anhydrous DMF at 0°C under argon atmosphere was added NaH 60% (70.7 mg, 1.84 mmol) portion wise. After 15 min, tert-butyl N-(6-bromohexyl) carbamate (517 mg, 1.84 mmol) in 8 mL of anhydrous DMF was added dropwise and stirred for 18 h at room temperature. The crude product was diluted in saturated aqueous $NaHCO_3$ and extracted with CH_2Cl_2. The organic phases were dried over Na_2SO_4, and evaporated. The residue was purified by chromatography on a silica gel column (0% to 30% EtOAc in *n*-heptane) to afford a clear oil (307 mg; yield 72%). t_R = 6.71 min. ^{1}H RMN (400 MHz, DMSO-d_6) : δ 8.39-8.37 (m, 1H), 8.04-7.71 (m, 2H), 7.41-7.25 (m, 3 H), 7.11-6.96 (m, 2H), 6.83-6.71(m, 1H), 6.32-6.31 (m, 1H), 4.79-4.74 (m, 1H), 4.53-4.52 (m, 1H), 3.57-3.38 (m, 2H), 2.94-2.73 (m, 3H), 2.37-2.14 (m, 4H), 2.02-1.98 (m, 1H), 1.69-1.52 (m, 4H), 1.41-1.20 (m, 17H). ^{13}C (100 MHz, DMSO-d_6) : δ 165.3, 164.8, 155.5, 150.5, 141.6, 140.1, 139.8, 138.7, 137.4, 133.3, 133.1, 131.5, 130.8, 129.3, 128.8, 128.7, 128.5, 127.7, 127.3, 127.2, 127.1, 117.8, 117.6, 116.5, 115.5, 114.8, 108.5, 81.0, 79.1, 77.7, 77.2, 68.9, 68.2, 46.9, 46.1, 39.8, 32.7, 29.4, 28.2, 26.2, 25.5, 24.9, 22.5, 13.3.

^{par}MCF14. Compound **2** (14 mg, 0.03 mmol) was dissolved in a solution HCl 4N/Dioxane (400 µL) and was stirred 30 min at room temperature and then evaporated. The residue was dissolved in DMF (1 mL) under argon. Then 3-carboxy-PROXYL (6.7 mg, 0.036 mmol) and PyBOP (18.7 mg, 0.04 mmol) were added to the solution followed by DIEA (0.03 mL, 0.18 mmol). Then the resulting mixture was stirred for 1 h and evaporated. The expected compound was isolated by semi-preparative RP-HPLC on a Sunfire RP-C18 column using a linear gradient of solvent B in solvent A. Fractions containing the product were freeze-dried to afford a clear oil (10.7 mg; yield 55 %). t_R = 5.80 min. HRMS (EI) *m/z* calcd for $C_{36}H_{48}ClN_5O_4$ $[M+H]^+$ 649.3317, found : 649.3305.

^{par}dLVP

To a solution of (deamino-Cys1, Lys8)-Vasopressin trifluoroacetate (2.5 mg, 2.16 µmol) and 3-carboxy-PROXYL (0.48 mg, 2.6 µmol) in anhydrous DMF (100 µL) under argon atmosphere were added DIEA (2.15 µL, 12.9 µmol) and PyBOP (1.35 mg, 2.56 µmol), stirred for 1 h at room temperature and then evaporated. The expected compound was isolated by semi-preparative RP-HPLC on a Sunfire RP-C18 column using a linear gradient of solvent B in solvent A. Fractions containing the product were lyophilized to afford a white solid (1.7 mg ; yield 65%). t_R = 3.15 min. HRMS (EI) *m/z* calcd for $C_{55}H_{79}N_{13}O_{14}S_2$ $[M+H]^+$, 1209.5310, found : 1209.5315.

Supplementary references

(1) Bous, J.; Orcel, H.; Floquet, N.; Leyrat, C.; Lai-Kee-Him, J.; Gaibelet, G.; Ancelin, A.; Saint-Paul, J.; Trapani, S.; Louet, M.; Sounier, R.; Déméné, H.; Granier, S.; Bron, P.; Mouillac, B. Cryo-Electron Microscopy Structure of the Antidiuretic Hormone Arginine-Vasopressin V2 Receptor Signaling Complex. *Sci. Adv.* **2021**, *21* (7), eabg5628. https://doi.org/10.1101/2022.02.11.480047

(2) Wang, L.; Friesner, R. A.; Berne, B. J. Replica Exchange with Solute Scaling: A More Efficient Version of Replica Exchange with Solute Tempering (REST2). *The Journal of Physical Chemistry B* **2011**, *115* (30), 9431–9438. https://doi.org/10.1021/jp204407d.

(3) Patriksson, A.; van der Spoel, D. A Temperature Predictor for Parallel Tempering Simulations. *Physical Chemistry Chemical Physics* **2008**, *10* (15), 2073. https://doi.org/10.1039/b716554d.

(4) Marie-Céline Frantz, Lucie P. Pellissier, Elsa Pflimlin, Stéphanie Loison, Jorge Gandia Claire Marsol, Thierry Durroux, Bernard Mouillac, Jérôme A.J. Becker, Julie Le Merrer, Christel Valencia, Pascal Villa, Dominique Bonnet, Marcel Hibert. LIT-1, the first nonpeptide oxytocin receptor agonist that improves social interaction in a mouse model of autism. *J. Med. Chem* **2018**, *61*, 8670-8692.
https://doi: 10.1021/acs.jmedchem.8b00697